



# Sun-as-a-star Analyses of Various Solar Active Events Using H $\alpha$ Spectral Images Taken by SMART/SDDI

Takato Otsu<sup>1</sup>, Ayumi Asai<sup>2</sup>, Kiyoshi Ichimoto<sup>2</sup> , Takako T. Ishii<sup>2</sup>, and Kosuke Namekata<sup>3</sup>

<sup>1</sup> Department of Astronomy, Kyoto University, Sakyo, Kyoto, Japan; [totsu@kusastro.kyoto-u.ac.jp](mailto:totsu@kusastro.kyoto-u.ac.jp)

<sup>2</sup> Astronomical Observatory, Kyoto University, Sakyo, Kyoto, Japan

<sup>3</sup> ALMA Project, NAOJ, NINS, Osawa, Mitaka, Tokyo, Japan

Received 2022 August 1; revised 2022 September 27; accepted 2022 October 2; published 2022 November 10

## Abstract

Sun-as-a-star analyses in which observational data is spatially integrated are useful for interpreting stellar data. For future applications to stellar observations, we performed Sun-as-a-star analyses of H $\alpha$  spectra for various active events on the Sun, not only for flares and filament eruptions/surges on the solar disk, but also for eruptions of off-limb prominences using H $\alpha$  spectral images taken by the Solar Magnetic Activity Research Telescope/Solar Dynamics Doppler Imager at Hida Observatory, Kyoto University. All the analyzed events show emission relative to the pre-event state and the changes in their H $\alpha$  equivalent widths are all on the orders of  $10^{-4}$  Å. Sun-as-a-star H $\alpha$  spectra exhibit different features depending on the causes of the emission: (i) flares show emission at the H $\alpha$  line center, together with red asymmetry and line broadening, as reported in a previous study, (ii) filament eruptions with and without flares show emission near the H $\alpha$  line center, accompanied by blueshifted/redshifted absorption; notably, the disappearance of dark filaments leads to the apparent enhancement of the H $\alpha$  line center emission, and (iii) eruptions of off-limb prominences show blueshifted/redshifted emission. These spectral features enable us to identify the active phenomena on Sun-like stars. We have also found that even the filament eruptions showing redshifted absorptions in Sun-as-a-star H $\alpha$  spectra lead to coronal mass ejections (CMEs). This result suggests that even if the falling components of stellar filament eruptions are detected as redshifted absorptions in H $\alpha$  spectra, such stellar filament eruptions may also develop into CMEs.

*Unified Astronomy Thesaurus concepts:* Solar flares (1496); Stellar flares (1603); Solar filament eruptions (1981); Solar prominences (1519); Solar coronal mass ejections (310); Stellar coronal mass ejections (1881); Solar chromosphere (1479)

## 1. Introduction

Solar flares are explosive brightenings in the solar atmosphere. They are thought to be caused by the conversion of magnetic energy into kinetic, thermal, and nonthermal energies via magnetic reconnection (Shibata & Magara 2011). In addition, filament/prominence eruptions and coronal mass ejections (CMEs) sometimes accompany solar flares. The interaction between CMEs and Earth’s magnetosphere could produce geomagnetic storms, which have serious impacts on modern human life (e.g., Airapetian et al. 2020; Cliver et al. 2022).

Like the Sun, various stars also show sudden brightenings called stellar flares. In recent years, superflares—which are stellar flares emitting more than  $10^{33}$  erg—have been observed even in stars similar to the Sun (Maehara et al. 2012; Shibayama et al. 2013; Tu et al. 2020; Okamoto et al. 2021). In order to understand flares including superflares in a unified way, stellar flares are being investigated actively (e.g., Kowalski et al. 2013; Tsoboi et al. 2016; Honda et al. 2018; Notsu et al. 2019; Vida et al. 2019; Muheki et al. 2020; Namekata et al. 2020; Maehara et al. 2021; Namekata et al. 2022a, 2022b). Stellar superflares may be accompanied by much larger CMEs than those of the Sun, which are thought to have severe impacts on the exoplanets around the host stars (e.g., Airapetian et al. 2020). Consequently, superflares and

their associated CMEs have been gathering attention, not only from a physical viewpoint, but also from the perspective of the habitability of exoplanets.

The surface of the Sun can be observed with high spatial resolution, while the surfaces of distant stars cannot be resolved spatially. In recent years, the spatially resolved data of the Sun have been utilized to aid the analysis of stellar data (e.g., Harra et al. 2016; Toriumi et al. 2020; Veronig et al. 2021; Namekata et al. 2022a, 2022b; Toriumi & Airapetian 2022; Xu et al. 2022). For comparison with the stellar data, solar data are integrated spatially, and such an analysis is called “Sun-as-a-star analysis”. Namekata et al. (2022a) performed Sun-as-a-star analyses using H $\alpha$  images of two solar flares accompanied by filament eruption/surge to interpret the H $\alpha$  spectra of a stellar flare. Since both solar and stellar spectra have similar characteristics, the authors concluded that a stellar filament eruption associated with a superflare had been detected. In addition, Namekata et al. (2022c) analyzed the Sun-as-a-star H $\alpha$  spectrum of an M-class solar flare that exhibited dominant emission from flare ribbons, and they showed that red asymmetry and line broadening can be seen even in a Sun-as-a-star spectrum, providing evidence of chromospheric condensation. This is how Sun-as-a-star analyses of H $\alpha$  spectra are useful for investigating the dynamics of flares and plasmas on a stellar surface. Also, in contrast to extreme ultraviolet (EUV) radiation, which is also useful for studying stellar activities, especially stellar CMEs (Harra et al. 2016; Xu et al. 2022) but cannot reach Earth from distant stars due to interstellar absorption (Rumph et al. 1994), we can observe H $\alpha$  radiation even coming from distant stars. It is therefore



Original content from this work may be used under the terms of the [Creative Commons Attribution 4.0 licence](#). Any further distribution of this work must maintain attribution to the author(s) and the title of the work, journal citation and DOI.

**Table 1**  
List of Events Analyzed in This Paper

Event	Date (UT)	GOES Peak Time (UT)	GOES Class	Location	Event Features	CME
(1)	2017 Apr 2	02:46:00	C8.0	S12 W08	Flare + surge	No?
(2)	2017 Apr 2	08:02:00	M5.3	N12 W59	Flare + eruption	Yes
(3)	2017 Sep 8	07:49:00	M8.1	S09 W70	Flare (two step) + eruption	No?
(4)	2021 Apr 19–20	23:42:00	M1.1	S24 E14	Flare + coronal rain?	Yes
(5)	2016 Nov 5	04:52:00	B1.1	N08 W32	Two-ribbon flare + filament eruption	Yes
(6)	2017 Feb 19	05:41:00	B3.0	N11 E15	Two-ribbon flare + filament eruption	Yes
(7)	2017 Apr 23	05:55:00	B1.8	N13 E33	Two-ribbon flare + filament eruption	Yes
(8)	2017 June 19			NE limb	Prominence eruption	Yes
(9)	2021 May 5			NE limb	Prominence eruption (two step)	Yes

**Note.** The flaring footpoints of event (8) and event (9) were occulted so we did not include the GOES class and peak time of these two events in Table 1. The occurrence of CMEs for events (1)–(4), event (8), and event (9) is based on SOHO/LASCO data, and events (5)–(7) are from Seki et al. (2019b). The term “No?” means that we cannot decide the occurrence of CMEs from SOHO/LASCO data. Note that although event (4) was not associated with any H $\alpha$  eruptions, it would be followed by a hotter eruption.

important to investigate H $\alpha$  spectra by performing Sun-as-a-star analyses not only for flares and filament eruptions/surges but also for various other active phenomena on the Sun.

So far, Sun-as-a-star analyses of H $\alpha$  spectra have been performed for only three solar active events (flares and filament eruptions/surges; Namekata et al. 2022a, 2022c). In this paper, we report the results of Sun-as-a-star analyses of H $\alpha$  spectra for various active events on the Sun. In addition to flares and filament eruptions/surges, there is a wide variety of chromospheric plasma phenomena—such as out-of-limb prominence eruptions (e.g., Parenti 2014) and post-flare loops (e.g., Jing et al. 2016)—and we have included these phenomena, which have not been analyzed previously from the Sun-as-a-star viewpoint. Our main goal is to clarify the correspondence between various active events and the characteristics of the H $\alpha$  spectra in Sun-as-a-star analyses, for future applications to stellar observations. We mainly followed the method of Sun-as-a-star analyses described by Namekata et al. (2022a), while we incorporated our own calibration method in this paper. We introduce the observational data in Section 2 and explain the analytical method in Section 3. In Section 4, we report the results and discuss them. Finally, we present a summary and implications for stellar observations in Section 5.

## 2. Observations

The Solar Dynamics Doppler Imager (SDDI; Ichimoto et al. 2017) is installed on the Solar Magnetic Activity Research Telescope (SMART; Ueno et al. 2004) at Hida Observatory, Kyoto University. It takes full-disk solar images at 73 wavelengths from the H $\alpha$  line center  $-9.0\text{ \AA}$  to the H $\alpha$  line center  $+9.0\text{ \AA}$  with a time cadence of 12–16 s and a pixel size of  $1''.23$ . SDDI has been observing the Sun routinely since 2016 May and has stored H $\alpha$  spectral images of various active events.

We have selected relatively prominent events to study in this paper: flares with GOES (Geostationary Operational Environmental Satellites) X-ray classes of  $\geq C8.0$  and plasma eruptions with large spatial scales (on the order of approximately 100 Mm). We excluded some events because of clouds or extremely poor seeing. We ultimately selected nine events. For these events, we summarize in Table 1 the dates of the observations, the GOES peak time, GOES class, location, and event features. We also summarize in Table 1 the occurrence of CMEs based on the data of the Large Angle and Spectrometric

Coronagraph (LASCO; Brueckner et al. 1995) on board the Solar and Heliospheric Observatory (SOHO) and the catalog of filament disappearance in Seki et al. (2019b). In addition to the SDDI data, for some events we used data taken with the Atmospheric Imaging Assembly (AIA; Lemen et al. 2012) on board the Solar Dynamics Observatory (SDO; Pesnell et al. 2012) to ensure the event scenarios. In the following, we provide observational classifications of the events studied in this paper. Note that this classification is not essential but is just convenient for explanation. The details of each event are given in Section 4.

Events (1)–(4) were associated with flares ( $\geq C8.0$ ). Event (1) is the same as that analyzed by Namekata et al. (2022a). Although this event has already been analyzed in detail, it is included in this paper again with the intent of comparing it to other events. Events (5)–(7) were filament eruptions associated with weak flares (B class). In these three events, dark filaments were observed on the solar disk in the H $\alpha$  line center images, and they erupted with partial drainage. Events (8) and (9) were prominence eruptions to the outside of the solar limb. The footpoints of the flares from these events were occulted, and their GOES data are therefore not summarized in Table 1.

## 3. Method

Because the brightening of a solar flare is much smaller than the radiation from the full solar disk, it is difficult to identify clear changes in Sun-as-a-star spectra that are simply integrated over the full disk. We therefore integrated the H $\alpha$  spectra over partial target regions (TRs) which contain the active events we consider. This is equivalent to assuming that there are no other variations except for that in the TR. We converted these spatially integrated spectra in TRs to virtual Sun-as-a-star spectra (see Namekata et al. 2022a) by normalizing them with the full-disk integrated solar continuum. The details of this method are as follows.

First, we define  $f(t, \lambda, A)$  as an H $\alpha$  spectrum that is simply integrated over a region denoted by A:

$$f(t, \lambda, A) = \int_A I(t, \lambda, x, y) dx dy, \quad (1)$$

where  $I(t, \lambda, x, y)$  is the intensity as a function of the time of the observation  $t$ , the wavelength  $\lambda$ , and the spatial position  $(x, y)$ . In order to suppress intensity fluctuations coming from temperature variations of the SDDI, we normalized  $f(t, \lambda, A)$

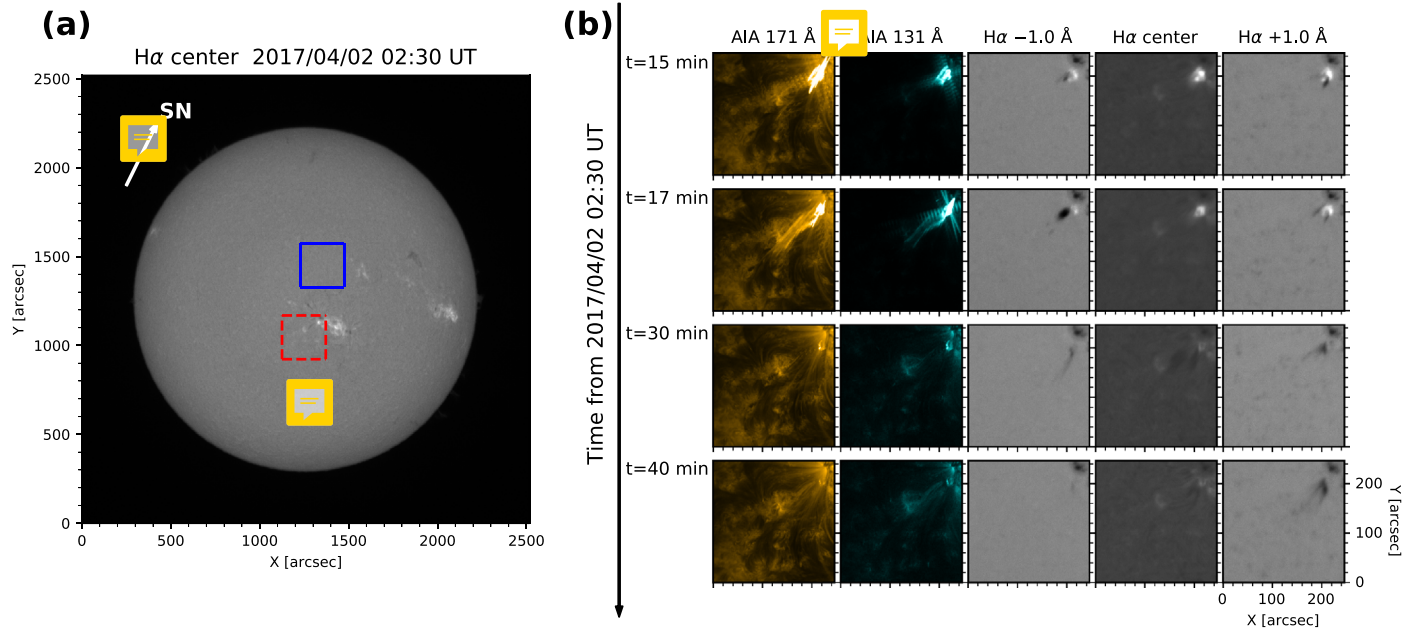


**Figure 1.** Overview of event (1), which occurred on 2017 April 2. (a) A full-disk solar image at the H $\alpha$ -center wavelength observed by SMART/SDDI. Celestial north is up, and west is to the right. The red dashed region is a TR, and the blue solid region is a QR. The direction of the solar north is shown by the white arrow labeled SN. (b) The time evolution of the C8.0 flare on 2017 April 2. The field of view in each panel corresponds to the TR in Figure 1(a). In each row, the images at the times  $t = 15, 17, 30$ , and  $40$  minutes measured from 02:30 UT on 2017 April 2 are shown from top to bottom. In each column, the images AIA 171 Å, AIA 131 Å, H $\alpha$  - 1.0 Å, H $\alpha$  center, and H $\alpha$  + 1.0 Å are shown from left to right.

by its continuum level at each time:

$$F(t, \lambda, A) = \frac{f(t, \lambda, A)}{f(t_0, \lambda_{\text{cont}}, A)} \times f(t_0, \lambda_{\text{cont}}, A), \quad (2)$$

where  $t_0$  is a pre-event time and  $\lambda_{\text{cont}}$  is a continuum wavelength near the H $\alpha$  line. The next step is normalization by a quiet region (QR). We used Equation (2) to obtain  $F(t, \lambda, A = \text{TR})$  and  $F(t, \lambda, A = \text{QR})$ . We then calculated the H $\alpha$  spectrum  $F_{\text{TR}}(t, \lambda)$  integrated over the TR and normalized by the QR data:

$$F_{\text{TR}}(t, \lambda) = \frac{F(t, \lambda, A = \text{TR})}{F(t, \lambda, A = \text{QR})} \times F(t_0, \lambda, A = \text{QR}). \quad (3)$$

This normalization suppresses influences coming from the observational environment, such as from changes in solar altitudes or from the Earth's atmospheric fluctuations. After the two normalizations given by Equations (2) and (3), we subtracted the pre-event data from  $F_{\text{TR}}(t, \lambda)$  to obtain the change due to the active events:

$$\Delta F_{\text{TR}}(t, \lambda) = F_{\text{TR}}(t, \lambda) - F_{\text{TR}}(t_0, \lambda), \quad (4)$$

Finally, we normalized  $\Delta F_{\text{TR}}(t, \lambda)$  by the full-disk solar continuum  $F(t_0, \lambda_{\text{cont}}, A = \text{full disk})$ :

$$\Delta S(t, \lambda) = \Delta F_{\text{TR}}(t, \lambda) / F(t_0, \lambda_{\text{cont}}, A = \text{full disk}). \quad (5)$$

The resulting normalized pre-event-subtracted H $\alpha$  spectrum  $\Delta S(t, \lambda)$  represents the ratio of the spectral changes coming from active events to the solar irradiance (full-disk continuum). If there is no other variation except for the target event, we can calculate  $\Delta S(t, \lambda)$  by using the observational data as if we were observing the Sun as a distant star. Therefore,  $\Delta S(t, \lambda)$  can be regarded as a Sun-as-a-star H $\alpha$  spectrum. We also calculated the difference equivalent width:  $\Delta \text{EW}_{\text{H}\alpha \pm \Delta \lambda} = \int_{\text{H}\alpha - \Delta \lambda}^{\text{H}\alpha + \Delta \lambda} \Delta S(t, \lambda) d\lambda$  where

H $\alpha \pm \Delta \lambda$  means the wavelength of H $\alpha$  line center  $\pm \Delta \lambda$  (Å). The difference equivalent width corresponds to the total change in the H $\alpha$  spectrum.



#### 4. Results and Discussion

Here, we introduce the time evolution of each of the nine events in spatially resolved images as well as the Sun-as-a-star H $\alpha$  spectra  $\Delta S(t, \lambda)$  of the nine events illustrated as dynamic spectra, i.e., as color maps of  $\Delta S(t, \lambda)$ . We also show the difference equivalent widths  $\Delta \text{EW}_{\text{H}\alpha \pm \Delta \lambda}$  and the GOES soft X-ray (SXR) light curves. We discuss the causes of the H $\alpha$  spectral formations from the Sun-as-a-star viewpoint by referring to the spatially resolved images. We use the line centers calculated by fitting quadratic functions to the line cores of quiet region data as the H $\alpha$  line center 6562.8 Å in the dynamic spectra. The absolute wavelengths of the H $\alpha$  spectra observed by SMART/SDDI are not accurate because the Lyot filter, which is the main component of SMART/SDDI, experiences temperature drift. Therefore, corrections to the wavelength zero-point are necessary in order to obtain accurate Doppler velocities.

##### 4.1. Event (1), a C8.0 Flare on 2017 April 2

Figure 1 shows an overview of event (1). In this event, a C8.0 flare occurred on 2017 April 02:30 UT in NOAA 12645 near the disk center (the red dashed region in Figure 1(a)). This flare was followed by an H $\alpha$  surge (Figure 1(b)).

Figure 2 shows the result of the Sun-as-a-star analysis of the H $\alpha$  spectra of this C8.0 flare. In the dynamic spectrum (Figure 2(a)), the emission appears near the H $\alpha$  line center. In the early phase of this emission, it shows line broadening. A strongly shifted absorption—transforming from a blueshift to a redshift—follows this emission. This strongly shifted absorption in the dynamic spectrum corresponds to the plasma

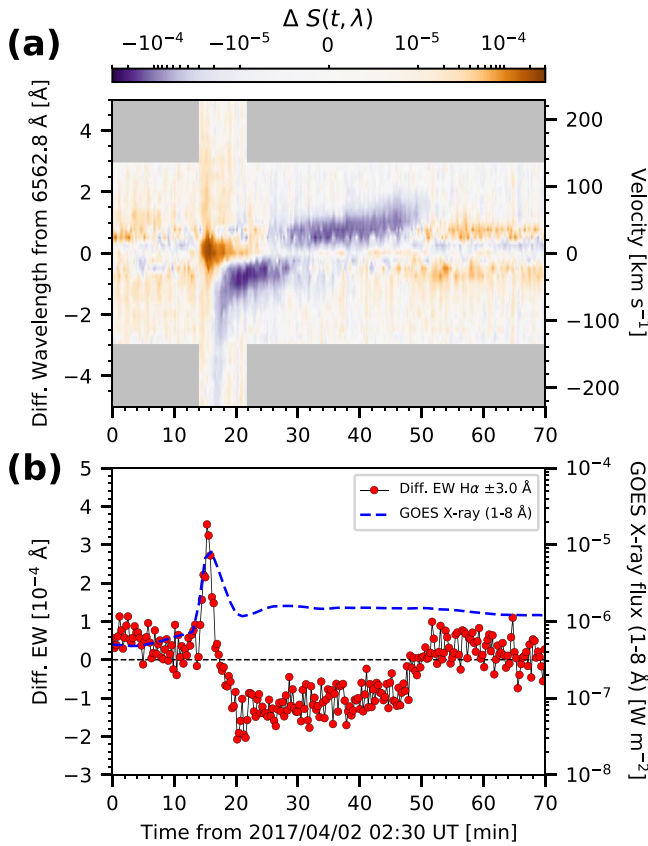


**Figure 2.** (a) The time series of the Sun-as-a-star H $\alpha$  spectra (dynamic spectrum) and (b) the light curves of event (1), the C8.0 flare on 2017 April 2. In panel (a), the left vertical axis is the difference in wavelength from the H $\alpha$  line center in units of Angstrom, and the right vertical axis is the corresponding Doppler velocity in units of kilometers per second. The horizontal axis is the time measured from 02:30 UT on 2017 April 2 in units of minutes. The color map shows  $\Delta S(t, \lambda)$ , where  $\Delta S(t, \lambda)$  represents the ratio of the changes in the pre-event-subtracted spatially integrated H $\alpha$  spectra to the full-disk continuum (see Equation (5)). The orange and purple regions correspond to emission and absorption, respectively. In the gray regions, there is no available data. Panel (b) shows the differenced equivalent widths of H $\alpha \pm 3.0$  Å as red circles and the GOES soft X-ray (1–8 Å) flux plotted as a blue dashed line. The horizontal axis is the same as that in panel (a). The horizontal dashed line represents the zero level of differenced equivalent width.

eruption and the downflow on the solar disk, i.e., the surge. The  $\Delta EW_{H\alpha \pm 3.0\text{\AA}}$  also shows strong absorption (on the order of  $\times 10^{-4}$  Å), and its time evolution deviates from the GOES SXR light curve (Figure 2(b)). The flaring amplitude is  $\sim 3 \times 10^{-4}$  Å, and the amplitude of the absorption is  $\sim 2 \times 10^{-4}$  Å.

These results are essentially consistent with the same analysis of the same event by Namekata et al. (2022a; see their Supplementary Information for a more detailed analysis of this event.). This consistency indicates the robustness of the Sun-as-a-star analysis method.

#### 4.2. Event (2), an M5.3 Flare on 2017 April 2

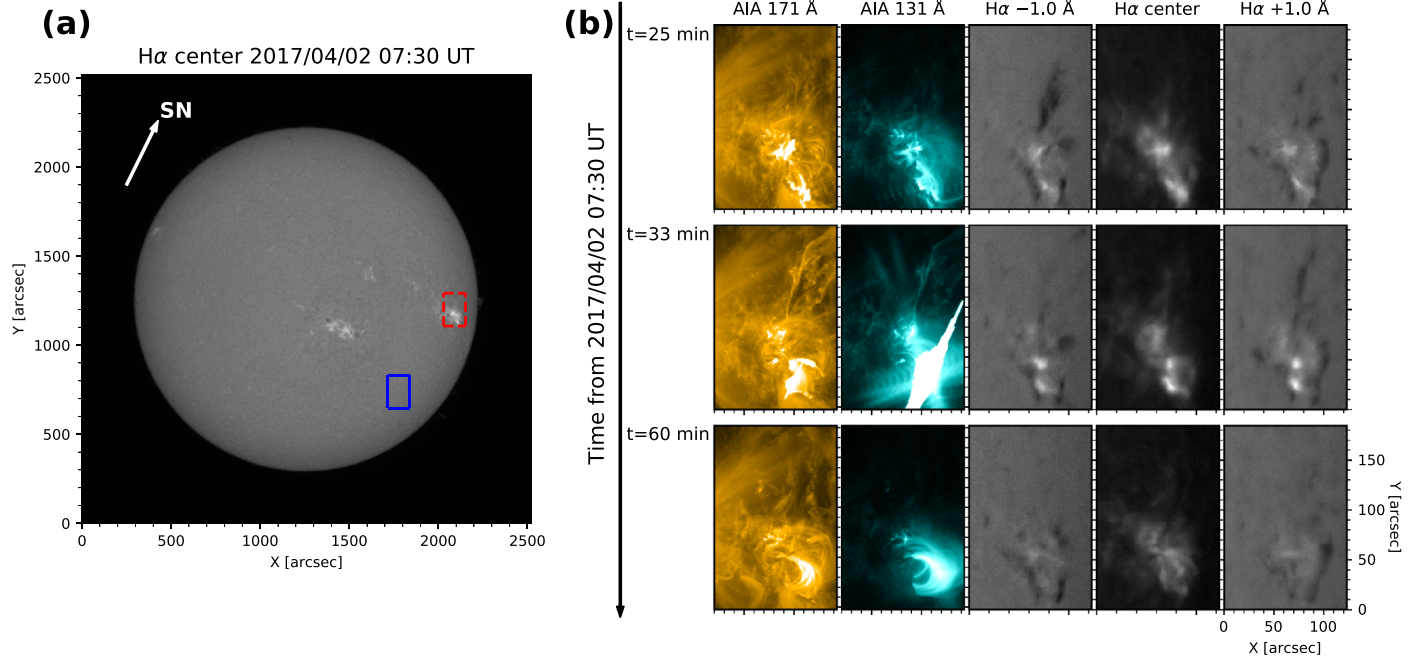
Figure 3 shows an overview of event (2). In this event, an M5.3 flare occurred on 2017 April 2 07:30 UT in NOAA 12644 near the solar limb (the red dashed region in Figure 3(a)). This flare was associated with a filament eruption (Figure 3(b)). After the GOES peak time of this flare, a clear cusp-like structure was observed in the SDO/AIA image (Figure 3(b),  $t = 60$  minutes).

Figure 4 shows the result of the Sun-as-a-star analysis of the H $\alpha$  spectra of this M5.3 flare. In the dynamic spectrum (Figure 4(a)), long-lasting emission appears near the H $\alpha$  line center. This emission extends up to  $\pm 2$  Å. Corresponding to the filament eruption on the disk, a blueshifted absorption appears in the dynamic spectrum. However, even though the spatial scales of the eruptions are the same,  $\sim 100$  Mm for both event (1) and event (2), the strength of the absorption in event (2) is weaker than that in event (1). This would be the result of cancellation between the emission due to the flare and the absorption by the erupted plasma. In this event, the filament erupted almost perpendicular to the line-of-sight (LOS) direction, with a very small LOS velocity. When the LOS velocity is very small, the filament appears near the H $\alpha$  line center, which is where the emission due to the flare appears, and absorption from the filament can cancel some of the emission from the flare. Moreover, near the H $\alpha$  line center, where the background H $\alpha$  intensity is very small, the degree of absorption from the filament is also decreased dramatically compared to cases in which the filament appears in the far wing of the H $\alpha$  line. Therefore, we also suggest that filament components are not dominant compared to the flare in this case, probably because the filament did not have a large contrast compared to the background due to its small LOS velocity (or possibly small density). In addition, the  $\Delta EW_{H\alpha \pm 3.0\text{\AA}}$  does not show any absorption. The flaring amplitude is  $\sim 4 \times 10^{-4}$  Å. The time evolution of the  $\Delta EW_{H\alpha \pm 3.0\text{\AA}}$  is similar to the GOES SXR light curve; for example, their timescales are comparable in each of the impulsive rising and gradual decay phases and their peaks are almost simultaneous (Figure 4(b)). The similarity of the H $\alpha$  and the GOES SXR light curves is also reported in the Sun-as-a-star analysis of a flare by Namekata et al. (2022c).

#### 4.3. Event (3), an M8.1 flare on 2017 September 8

Figure 5 shows an overview of event (3). In this event, an M8.1 class flare occurred on 2017 September 8 07:30 UT in NOAA 12673 near the solar limb (the red dashed region in Figure 5(a)). In the decay phase of the flare, a second brightening occurred. The first brightening was associated with a long ribbon-like structure and strong line broadening (Figure 5(b)  $t = 18$  minutes), while the second brightening was also associated with two small patches (Figure 5(b)  $t = 56$  and 60 minutes). The second brightening was followed by a filament eruption (Figure 5(b),  $t = 60$  minutes).

Figure 6 shows the result of the Sun-as-a-star analysis of the H $\alpha$  spectra of this M8.1 flare. In the dynamic spectrum (Figure 6(a)), two-step emission appears near the H $\alpha$  line center. The first emission has strong line broadening, while the second emission exhibits weaker line broadening than the first one. These emissions in the dynamic spectrum reflect features in the spatially resolved H $\alpha$  images (Figure 5(b)). As shown in the spatially resolved H $\alpha$  image (Figure 5(b)) a plasma eruption was indeed occurring, but the dynamic spectrum does not show clear absorption. This is probably because the filament erupted almost perpendicular to the LOS direction, as in event (2). The  $\Delta EW_{H\alpha \pm 3.0\text{\AA}}$  does not show any absorption; on the other hand, it clearly shows two-step brightening (Figure 6(b)). The flaring amplitudes are  $\sim 4 \times 10^{-4}$  Å for the first brightening and  $\sim 2 \times 10^{-4}$  Å for the second.

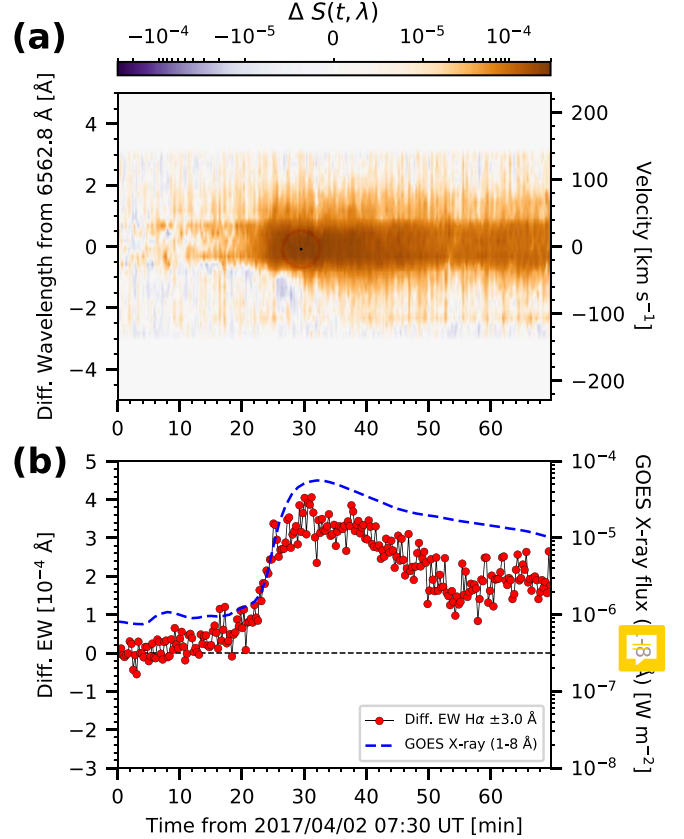


**Figure 3.** Overview of event (2), which occurred on 2017 April 2. (a) A full-disk solar image at the H $\alpha$ -center wavelength observed by SMART/SDDI. The red dashed region is a TR, and the blue solid region is a QR. Celestial north is up, and west is to the right. The direction of the solar north is shown by the white arrow labeled SN. (b) The time evolution of the M5.3 flare on 2017 April 2. The field of view in each panel corresponds to the TR in Figure 3(a). In each row, images at the times  $t = 25, 33, \text{ and } 60$  minutes measured from 07:30 UT on 2017 April 2 are shown from top to bottom. In each column, the images AIA 171  $\text{\AA}$ , AIA 131  $\text{\AA}$ , H $\alpha$  -1.0  $\text{\AA}$ , H $\alpha$  center, and H $\alpha$  +1.0  $\text{\AA}$  are shown from left to right.

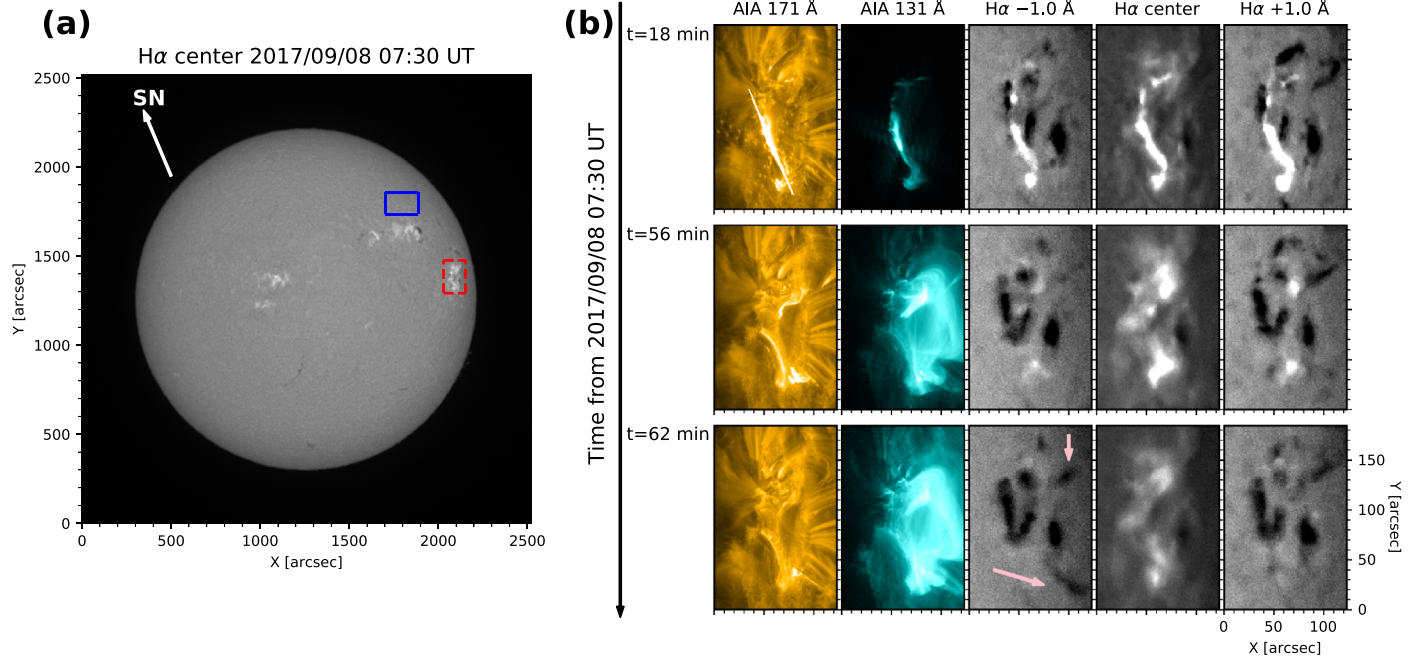
#### 4.4. Event (4), an M1.1 flare on 2021 April 19–20

Figure 7 shows an overview of event (4). In this event, an M1.1 class flare occurred on 2021 April 19 23:20 UT in NOAA 12816 near the disk center (the red dashed region in Figure 7(a), (b)). Although this flare was not followed by any H $\alpha$  plasma eruption, plasma downflows were observed in H $\alpha$  red-wing images during the decay phase of this flare. Prior to these downflows, a hot loop was observed in the AIA 171 and 131  $\text{\AA}$  images at the same position (Figure 7(b)). In a typical solar flare occurring on the solar disk, after the appearance of hot flare loops, cooled H $\alpha$  loops (*post-flare loops*) are observed as weak emissions at the H $\alpha$  line center. Moreover, cooled material moves downward along the post-flare loops (*coronal rain*), which is observed as absorption in the red wing of the H $\alpha$  line (e.g., Jing et al. 2016). Even in this event, the downflows in the flare-decay phase of event (4) may be coronal rain from the post-flare loop. However, since we cannot resolve the H $\alpha$  loop that is expected to exist in the *flare-decay phase*, there is another interpretation of these downflows (e.g., partial drainage of ejected hot plasmas).

Figure 8 shows the result of the Sun-as-a-star analysis of the H $\alpha$  spectra of this M1.1 flare. In the dynamic spectrum (Figure 8(a)), emission with a clear red asymmetry appears near the H $\alpha$  line center. When this emission has almost decayed, a redshifted absorption appears. This absorption corresponds to the plasma downflows, which may be coronal rain from the post-flare loop occurring during the decay phase of the flare (Figure 7(b)). The  $\Delta\text{EW}_{H\alpha \pm 3.0 \text{\AA}}$  also exhibits absorption after the peak of the flare (Figure 8(b)). The flaring amplitude is  $\sim 1.5 \times 10^{-4} \text{\AA}$ , and the amplitude of the absorption is  $\sim 0.5 \times 10^{-4} \text{\AA}$ .



**Figure 4.** The same as Figure 2, but for event (2), the M5.3 flare on 2017 April 2. We note that only H $\alpha$   $\pm 3.0 \text{\AA}$  data were available for performing the Sun-as-a-star analysis in this event.



**Figure 5.** Overview of event (3), which occurred on 2017 September 8. (a) A full-disk solar image at the H $\alpha$ -center wavelength observed by SMART/SDDI. Celestial north is up, and west is to the right. The red dashed is a TR, and the blue solid region is a QR. The direction of the solar north is shown by the white arrow labeled SN. (b) The time evolution of the M8.1 flare on 2017 September 8. The field of view in each panel corresponds to the TR in Figure 5(a). In each row, images at the times  $t = 18, 56$ , and  $62$  minutes measured from 07:30 UT on 2017 September 8 are shown from top to bottom. In each column, the images AIA 171  $\text{\AA}$ , AIA 131  $\text{\AA}$ , H $\alpha$   $-1.0$   $\text{\AA}$ , H $\alpha$  center, and H $\alpha$   $+1.0$   $\text{\AA}$  are shown from left to right. The pink arrows indicate plasma eruptions associated with the second brightening.

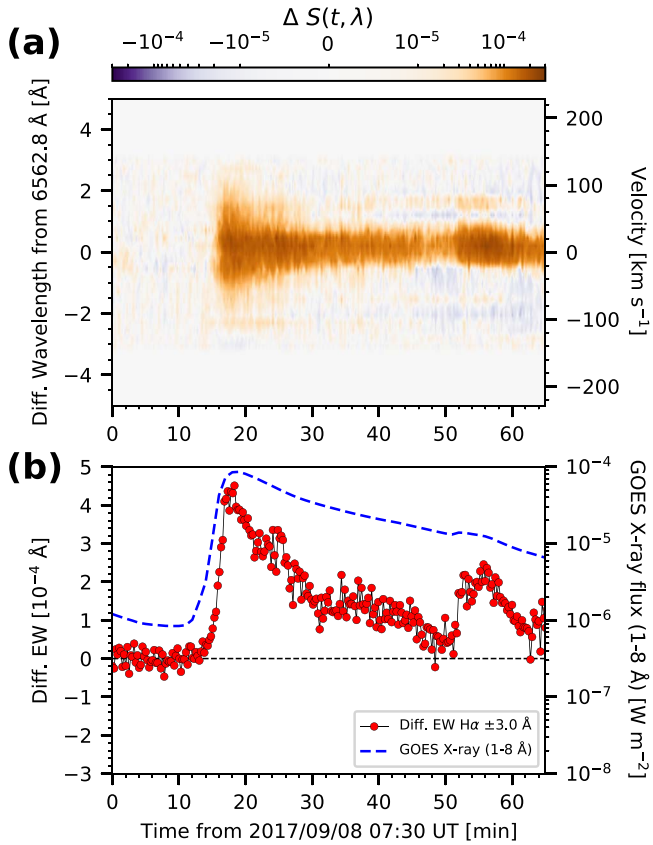


**Figure 6.** The same as Figure 2, but for event (3), the M8.1 flare on 2017 September 8. We note that only H $\alpha \pm 3.0$   $\text{\AA}$  data were available for performing the Sun-as-a-star analysis in this event.

#### 4.5. Event (5), a Filament Eruption on 2016 November 5

Figure 9 shows an overview of event (5). This event was analyzed from spatially resolved viewpoints by Seki et al. (2017). In this event, a filament eruption occurred on 2016 November 5 02:41 UT in the solar disk (the orange dashed – dotted region in Figure 9(a)). The dark filament was observed in the H $\alpha$  image before the eruption. In connection with the filament eruption, a two-ribbon flare also occurred, but it was distant from the filament eruption region. In order to model the phenomena associated with only a filament eruption, we integrated H $\alpha$  spectra over the TR that included the filament eruption alone (the red dashed region in Figure 9(a), (b)).

In events (5), (6), and (7), dark filaments were visible in the H $\alpha$  spectra before the eruptions. The contribution from the disappearance of such a dark filament to a Sun-as-a-star H $\alpha$  spectrum has not previously been investigated. In event (6) and event (7), the filament and the two-ribbon flare were colocated. Thus, it was difficult to separate the contributions from two-ribbon flares and from filament eruptions (the disappearance of the dark filament) to the formation of the Sun-as-a-star H $\alpha$  spectra in these two events. On the other hand, in event (5), the filament eruption occurred away from the two-ribbon flare (Figure 9). By using this spatial separation between the filament and the flare in event (5), we have been able to perform the Sun-as-a-star analysis for the filament eruption alone in event (5) and to investigate its contribution to the formation of the Sun-as-a-star H $\alpha$  spectra.

Figure 10 shows the result of the Sun-as-a-star analysis of H $\alpha$  spectra of this filament eruption. In the dynamic spectrum (Figure 10(a)), the emission with shifted absorptions appears near the H $\alpha$  line center. Since the H $\alpha$  spectra were integrated

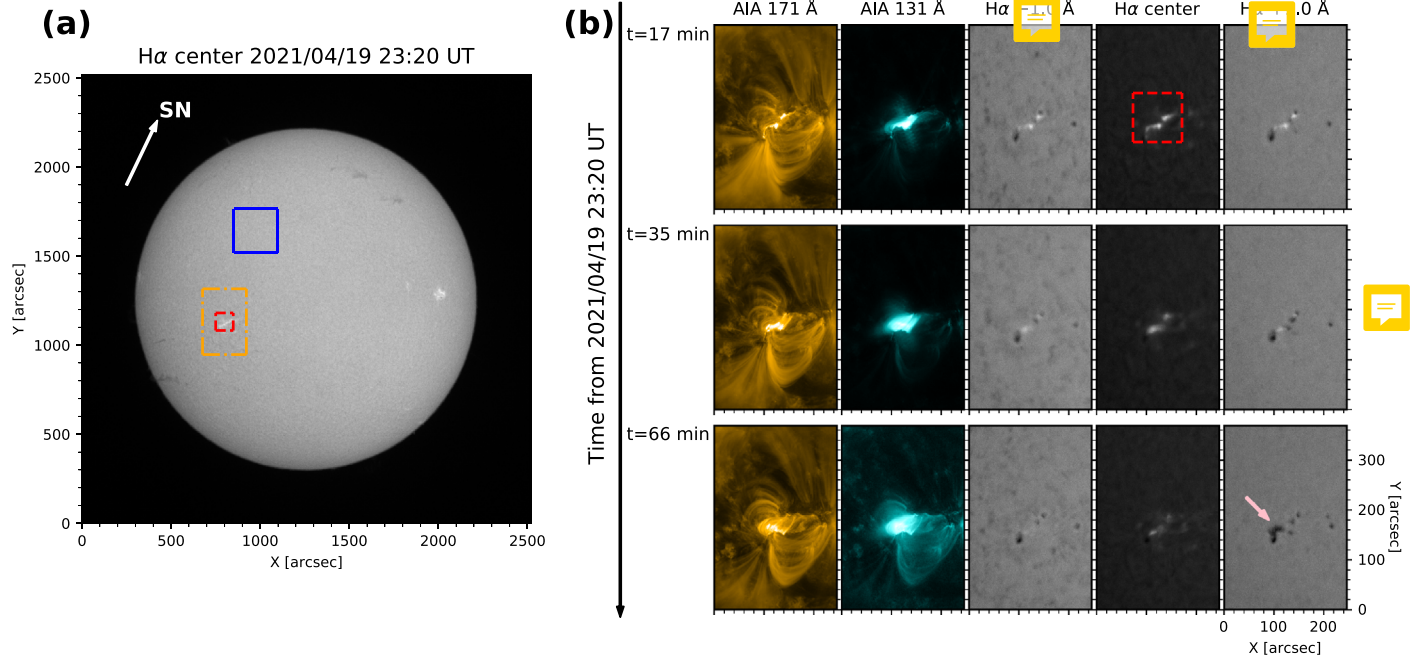


**Figure 7.** Overview of event (4), which occurred on 2021 April 19–20. (a) A full-disk solar image at the H $\alpha$ -center wavelength observed by SMART/SDDI. Celestial north is up, and west is to the right. The orange dashed–dotted region corresponds to the images in Figure 7(b), and the inner red dashed region is a TR. The blue solid region is a QR. The direction of the solar north is shown by the white arrow labeled SN. (b) The time evolution of the M1.1 class flare on 2021 April 19. The field of view in each panel corresponds to the orange dashed–dotted region in Figure 7(a). In each row, images at the times  $t = 17, 35$ , and  $66$  minutes measured from 23:30 UT on 2021 April 19 are shown from top to bottom. In each column, the images AIA 171  $\text{\AA}$ , AIA 131  $\text{\AA}$ , H $\alpha$  – 1.0  $\text{\AA}$ , H $\alpha$  center, and H $\alpha$  + 1.0  $\text{\AA}$  are shown from left to right. The red dashed region indicated in the H $\alpha$  center image at  $t = 17$  minutes is a TR. The pink arrow indicates plasma downflow during the decay phase of this M1.1 flare.

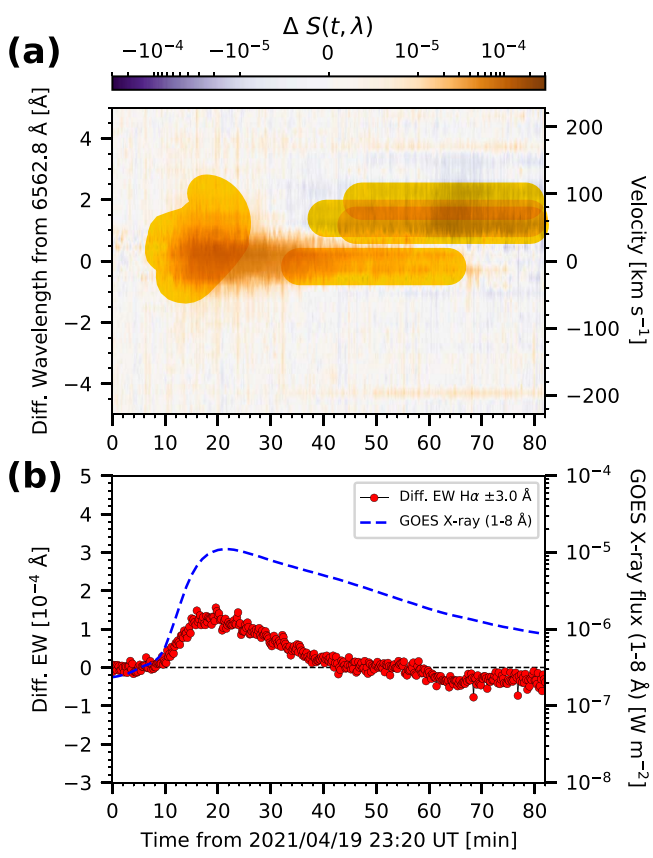


**Figure 8.** The same as Figure 2, but for event (4), the M1.1 flare on 2021 April 19–20.

over the TR that included the filament eruption alone, the emission seen in the H $\alpha$  line center is not due to the distant flare ribbon but instead is produced because the dark filament, which absorbed the background radiation at H $\alpha$  line center before the eruption, had disappeared from the line center. The blueshifted and redshifted absorptions correspond, respectively, to upward motions of the plasma and to partial drainage associated with the filament eruption (Figure 9(b)). The  $\Delta\text{EW}_{\text{H}\alpha \pm 3.0\text{\AA}}$  also shows absorption and emission (Figure 10(b)), the amplitudes of which are both  $\sim 1 \times 10^{-4}$   $\text{\AA}$ . The quantity  $\Delta\text{EW}_{\text{H}\alpha \pm 0.5\text{\AA}}$  is also calculated only over the range that includes the emission. The emission in  $\Delta\text{EW}_{\text{H}\alpha \pm 0.5\text{\AA}}$  appears at the almost same time as the absorption in  $\Delta\text{EW}_{\text{H}\alpha \pm 3.0\text{\AA}}$ . This simultaneity is consistent with the depiction that the emission comes from the disappearance of the dark filament.

How strong is the emission due to the disappearance of the dark filament compared to that from the two-ribbon flare? To address this question, we also calculated the differenced equivalent width for the two-ribbon flare alone. As shown in Figure 11, brightening from the disappearance of the dark filament is comparable to that from the two-ribbon flare. This result means that the contribution to the formation of a Sun-as-a-star H $\alpha$  spectrum from apparent emission by filament disappearance cannot be negligible compared to that from emission by a two-ribbon flare.

#### 4.6. Event (6), a Filament Eruption and a Two-ribbon Flare on 2017 February 19

Figure 12 shows an overview of event (6). In this event, a filament eruption occurred on 2017 February 19 05:11 UT

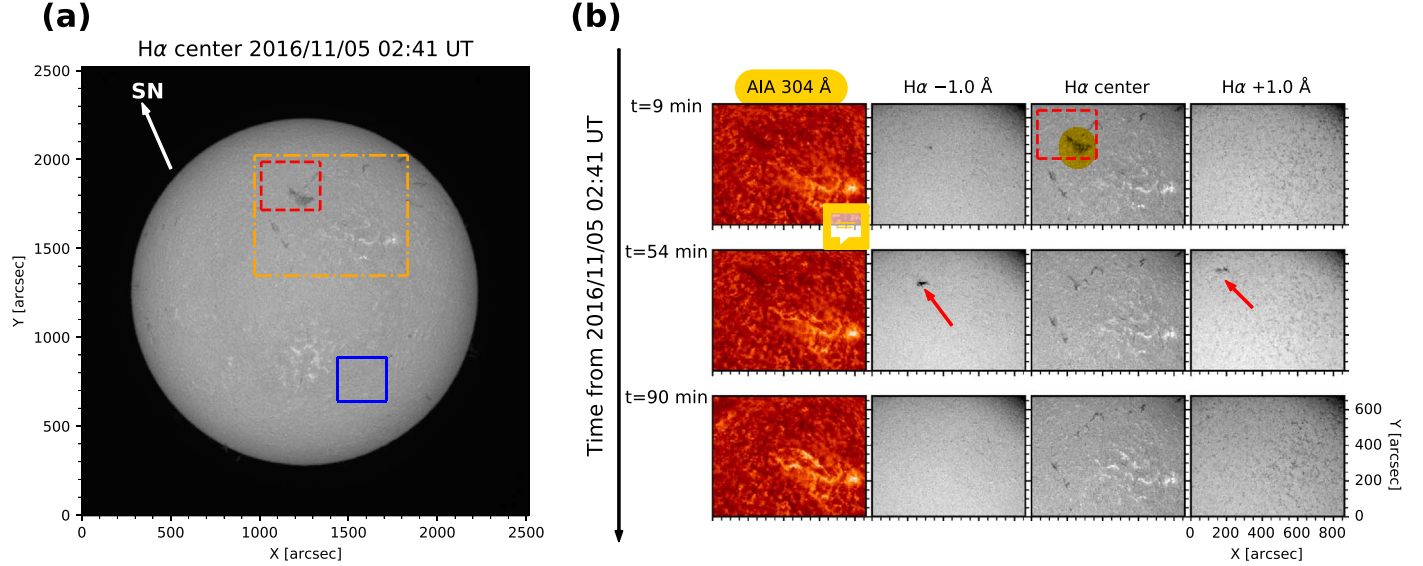


**Figure 9.** Overview of event (5), which occurred on 2016 November 5. (a) A full-disk solar image at the  $H\alpha$ -center wavelength observed by SMART/SDDI. Celestial north is up, and west is to the right. The orange dashed–dotted region corresponds to the images in Figure 9(b), and the blue solid region is a QR. The direction of the solar north is shown by the white arrow labeled SN. (b) The time evolution of the filament eruption on 2016 November 5. The field of view in each panel corresponds to the orange dashed–dotted region in Figure 9(a). In each row, images at the times  $t = 9, 54$ , and  $90$  minutes measured from 02:41 UT on 2016 November 5 are shown from top to bottom. In each column, the images AIA  $304 \text{ \AA}$ ,  $H\alpha - 1.0 \text{ \AA}$ ,  $H\alpha$  center, and  $H\alpha + 1.0 \text{ \AA}$  are shown from left to right. The red dashed region indicated in the  $H\alpha$  center image at  $t = 9$  minutes is a TR. The red arrow in the  $H\alpha - 1.0 \text{ \AA}$  image at  $t = 54$  minutes indicates the upward motion of the filament eruption. The red arrow in the  $H\alpha + 1.0 \text{ \AA}$  image at  $t = 54$  minutes indicates the plasma downflow associated with the filament eruption.

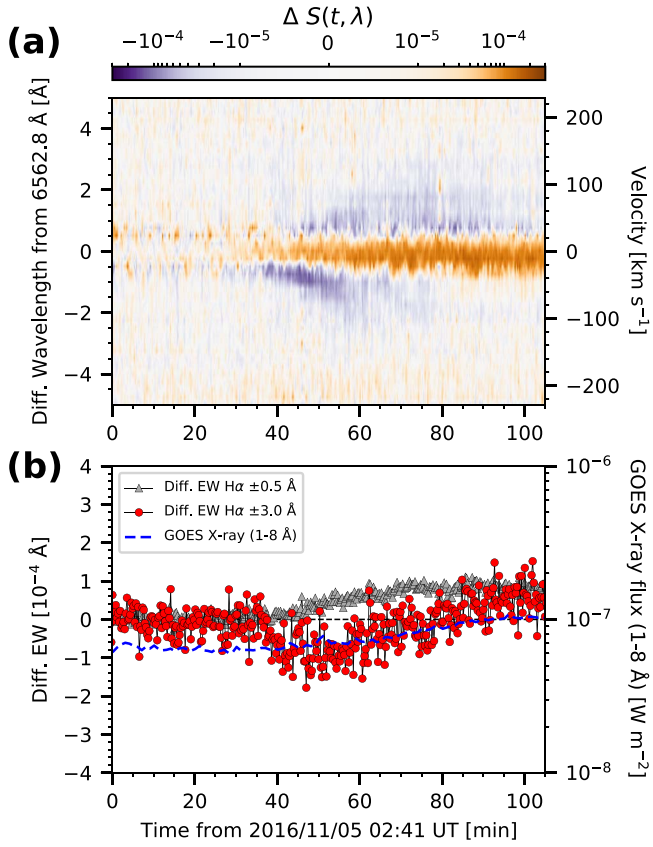


**Figure 10.** The same as Figure 2, but for the event (5), the filament eruption on 2016 November 5. In addition to the differenced equivalent widths of  $H\alpha \pm 3.0 \text{ \AA}$ , the differenced equivalent widths of  $H\alpha \pm 0.5 \text{ \AA}$  are also plotted in panel (b).

colocated with a two-ribbon flare (the red dashed region in Figure 12(a)).

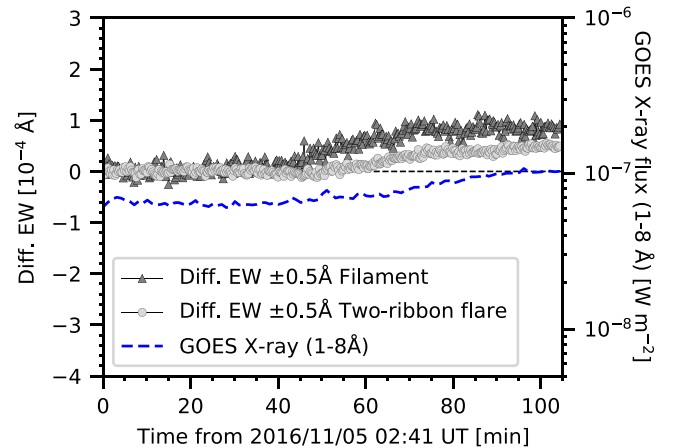


**Figure 11.** The contributions to the differenced equivalent widths from the filament eruption and the two-ribbon flare. The differenced equivalent widths of  $H\alpha \pm 0.5 \text{ \AA}$  for the filament eruption are plotted as gray triangles and for the two-ribbon flare as light gray circles. The GOES X-ray ( $1-8 \text{ \AA}$ ) flux is also plotted as a blue dashed line.

Figure 13 shows the result of the Sun-as-a-star analysis of the  $H\alpha$  spectra of this filament eruption and two-ribbon flare. In the dynamic spectrum (Figure 13(a)), emission with shifted absorptions appears near the  $H\alpha$  line center. In the same way as event (5), the blueshifted and redshifted absorptions correspond, respectively, to the upward motions of the plasma and to partial drainage associated with the filament eruption (Figure 12(b)). Before the fast blueshifted absorption, a slow blueshifted absorption appears in the dynamic spectrum. This slow absorption probably comes from the slow upward motions of the filaments before the eruption that was reported in many previous studies from spatially resolved viewpoints (Sterling & Moore 2004; Isobe & Tripathi 2006; Seki et al. 2017, 2019a). We also note that the fast blueshifted absorption is divided into

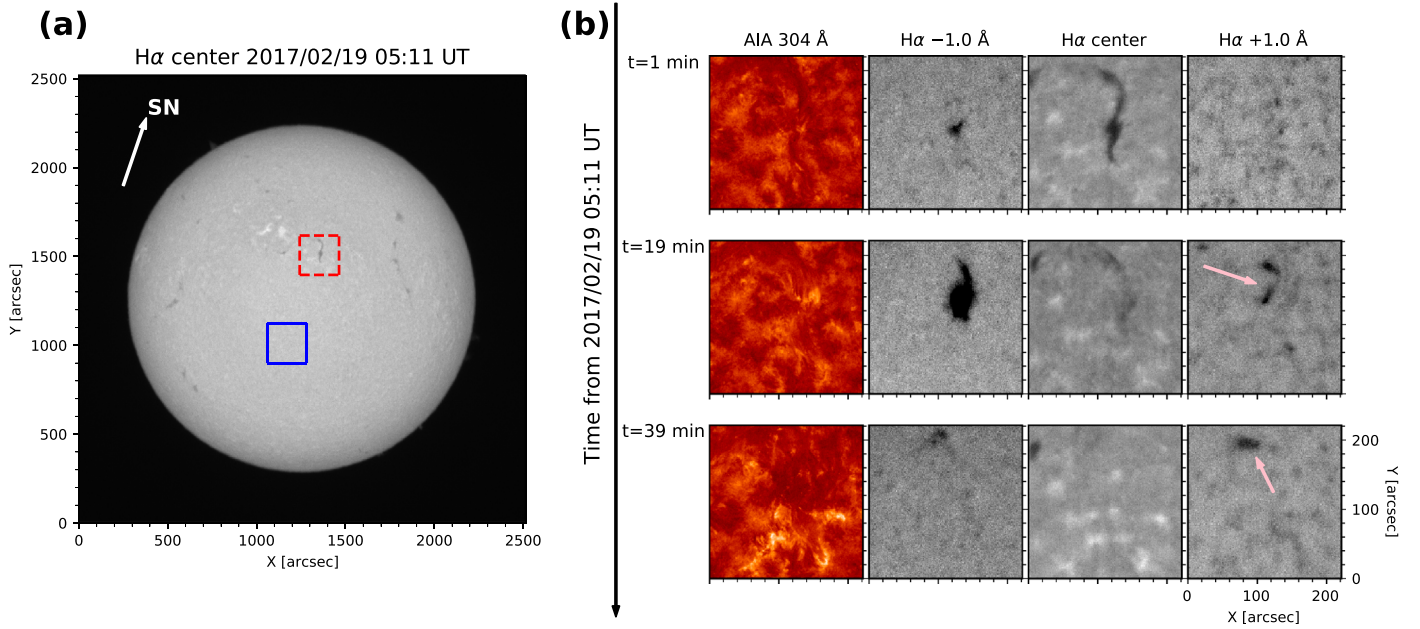


**Figure 12.** Overview of event (6), which occurred on 2017 February 19. (a) A full-disk solar image at the  $H\alpha$ -center wavelength observed by SMART/SDDI. Celestial north is up, and west is to the right. The red dashed region is a TR, and the blue solid region is a QR. The direction of the solar north is shown by the white arrow labeled SN. (b) The time evolution of the filament eruption on 2017 February 19. The field of view in each panel corresponds to the TR in Figure 12(a). In each row, images at the times  $t = 1, 9, \text{ and } 39$  minutes measured from 05:11 UT on 2017 February 19 are shown from top to bottom. In each column, the images AIA  $304 \text{ \AA}$ ,  $H\alpha - 1.0 \text{ \AA}$ ,  $H\alpha$  center, and  $H\alpha + 1.0 \text{ \AA}$  are shown from left to right. The pink arrows indicate plasma downflows associated with the filament eruption.

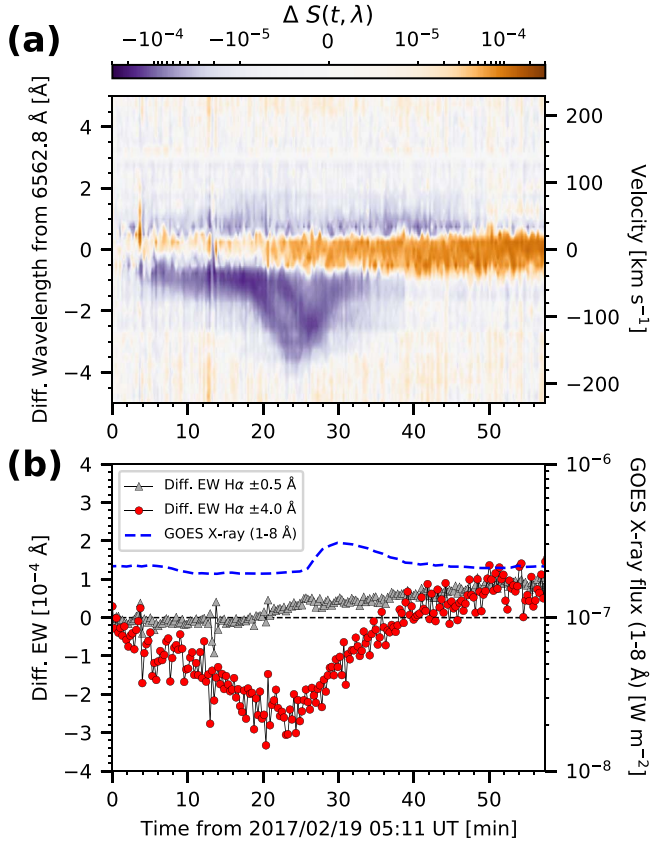


**Figure 13.** The same as Figure 2, but for event (6), the filament eruption and the two-ribbon flare on 2017 February 19. In addition to the differed equivalent widths of  $H\alpha \pm 3.0 \text{ \AA}$ , the differenced equivalent widths of  $H\alpha \pm 0.5 \text{ \AA}$  are also plotted as gray triangles in panel (b), as in Figure 10(b).

two stripes. The first stripe ends at about  $-4 \text{ \AA}$  ( $\sim -200 \text{ km s}^{-1}$ ), while the second stripe is decelerated and connected to the

redshifted absorption. The first stripe comes from erupted blobs that were accelerated to about  $-200 \text{ km s}^{-1}$  and finally faded away in the  $H\alpha$  images. The second stripe comes from erupted blobs that eventually fell back into the solar surface.

In this event, we include the two-ribbon flare in the TR. The AIA  $304 \text{ \AA}$  image shows a two-ribbon flare relatively clearly. Its counterparts are also observed in the  $H\alpha$  line center image (Figure 12(b)). Therefore, the emission near the  $H\alpha$  line center is a superposition of contributions from the two-ribbon flare and the disappearance of the dark filament. The quantity  $\Delta EW_{H\alpha \pm 4.0 \text{ \AA}}$  also shows the absorption and emission (Figure 13(b)), the amplitudes of which are  $\sim 3 \times 10^{-4}$  and  $\sim 1 \times 10^{-4} \text{ \AA}$ , respectively. The quantity  $\Delta EW_{H\alpha \pm 0.5 \text{ \AA}}$  is also calculated only over the range that includes the emission. The absorption in  $\Delta EW_{H\alpha \pm 4.0 \text{ \AA}}$  appears faster than the emission in  $\Delta EW_{H\alpha \pm 0.5 \text{ \AA}}$ . The faster appearance of this absorption may be the result of the slow upward motions of the filament before the fast eruption.

#### 4.7. Event (7), a Filament Eruption and a Two-ribbon Flare on 2017 April 23

Figure 14 shows an overview of event (7). In this event, a filament eruption occurred on 2017 April 23 05:00 UT colocated with a two-ribbon flare (the red dashed region in Figure 14(a)).

Figure 15 shows the result of the Sun-as-a-star analysis of the  $H\alpha$  spectra of this filament eruption. In the dynamic spectrum (Figure 15(a)), the emission with shifted absorptions appears near the  $H\alpha$  line center. In the same way as in event (5) and event (6), the blueshifted and redshifted absorptions correspond, respectively, to the upward motions of the plasma and partial drainage associated with the filament eruption (Figure 14(b)). In this event, we include the two-ribbon flare in the TR, as for event (6). The AIA  $304 \text{ \AA}$  image shows the two-ribbon flare relatively clearly, and its counterpart also appears

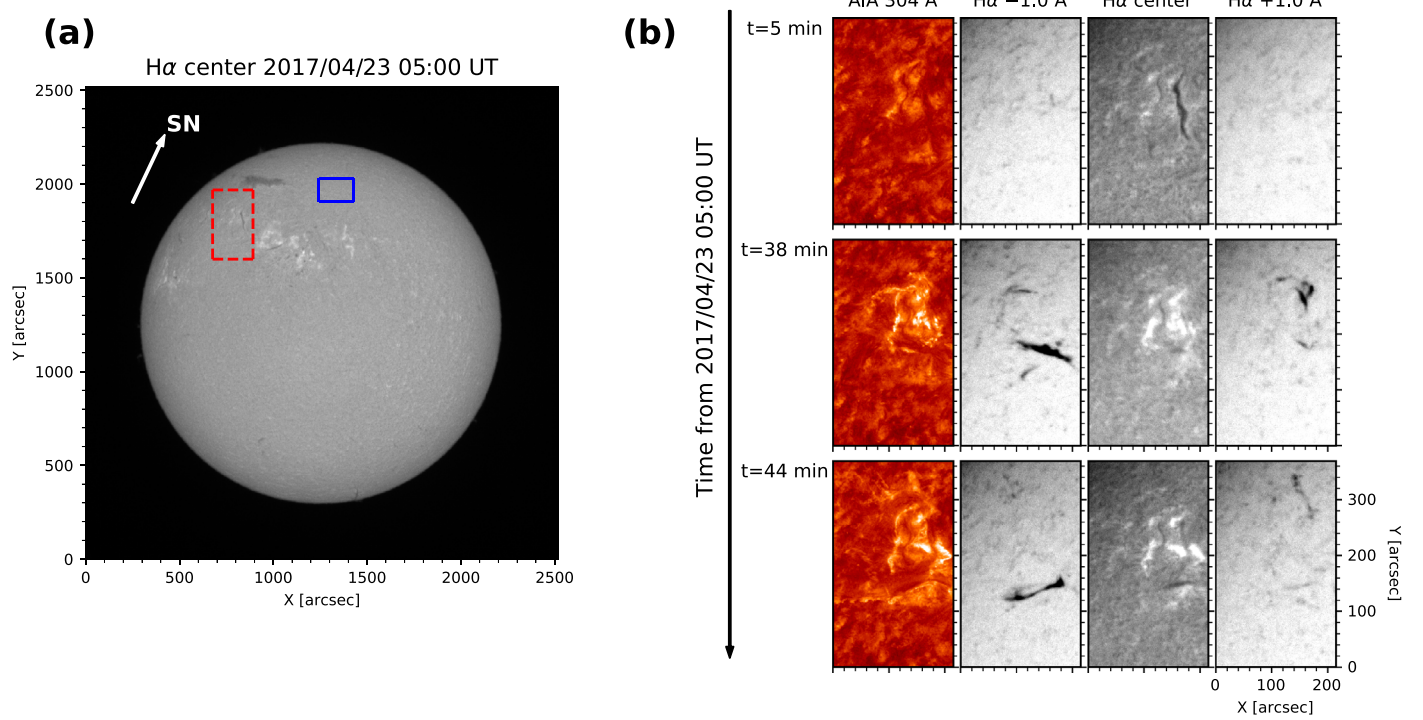


**Figure 14.** Overview of event (7), which occurred on 2017 April 23. (a) A full-disk solar image at the  $H\alpha$ -center wavelength observed by SMART/SDDI. Celestial north is up, and west is to the right. The red dashed region is a TR, and the blue solid region is a QR. The direction of the solar north is shown by the white arrow labeled SN. (b) The time evolution of the filament eruption on 2017 April 23. The field of view in each panel corresponds to the TR in Figure 14(a). In each row, images at the times  $t = 5, 38$ , and  $44$  minutes measured from 05:00 UT on 2017 April 23 are shown from top to bottom. In each column, the images AIA  $304 \text{ \AA}$ ,  $H\alpha - 1.0 \text{ \AA}$ ,  $H\alpha$  center, and  $H\alpha + 1.0 \text{ \AA}$  are shown from left to right.

clearly in the  $H\alpha$  line center image (Figure 14(b)). The emission near the  $H\alpha$  line center is therefore a superposition of contributions from the two-ribbon flare and the disappearance of the dark filament, as in event (6). The quantity  $\Delta EW_{H\alpha \pm 3.0 \text{ \AA}}$  also exhibits absorption and emission (Figure 15(b)), the amplitudes of which are  $\sim 3 \times 10^{-4}$  and  $\sim 1 \times 10^{-4} \text{ \AA}$ , respectively. The quantity  $\Delta EW_{H\alpha \pm 0.5 \text{ \AA}}$  is also calculated only over the range that includes the emission. The time evolution of the  $\Delta EW_{H\alpha \pm 0.5 \text{ \AA}}$  is similar to the GOES SXR light curve. This similarity is consistent with the clear two-ribbon flare in the  $H\alpha$  line.

#### 4.8. Event (8), a Prominence Eruption on 2017 June 19

Figure 16 shows an overview of event (8). In this event, a prominence eruption to the outside of the solar limb occurred on 2017 June 19 04:30 UT (the orange dashed–dotted region in Figure 16(a)). We integrated  $H\alpha$  spectra over the region outside of the solar disk (the red dashed region in Figure 16(b)). The  $H\alpha$  flare was not seen from Earth, so the footpoints of this event must be on the backside of the solar limb.

Figure 17 shows the result of the Sun-as-a-star analysis of the  $H\alpha$  spectra of this prominence eruption. Note that there are no pre-event data before 2017 June 19 04:30 UT because calibration frames were being taken. We have therefore used post-event data (after this event) in place of the pre-event data in analyzing this event. In the dynamic spectrum (Figure 17(a)), strongly shifted emission appears, which transforms from a blueshift to a redshift. In this event, the prominence erupted beyond the solar limb, with the LOS velocity approaching Earth. Part of the erupted plasma subsequently fell onto the

solar surface, with the LOS velocity moving away from Earth (Figure 16(b)). The shifted emission corresponds to this series of plasma motions outside the solar limb. The quantity  $\Delta EW_{H\alpha \pm 3.0 \text{ \AA}}$  also shows the emission (Figure 17(b)), with an amplitude of  $\sim 3 \times 10^{-4} \text{ \AA}$ .

#### 4.9. Event (9), a Prominence Eruption on 2021 May 5

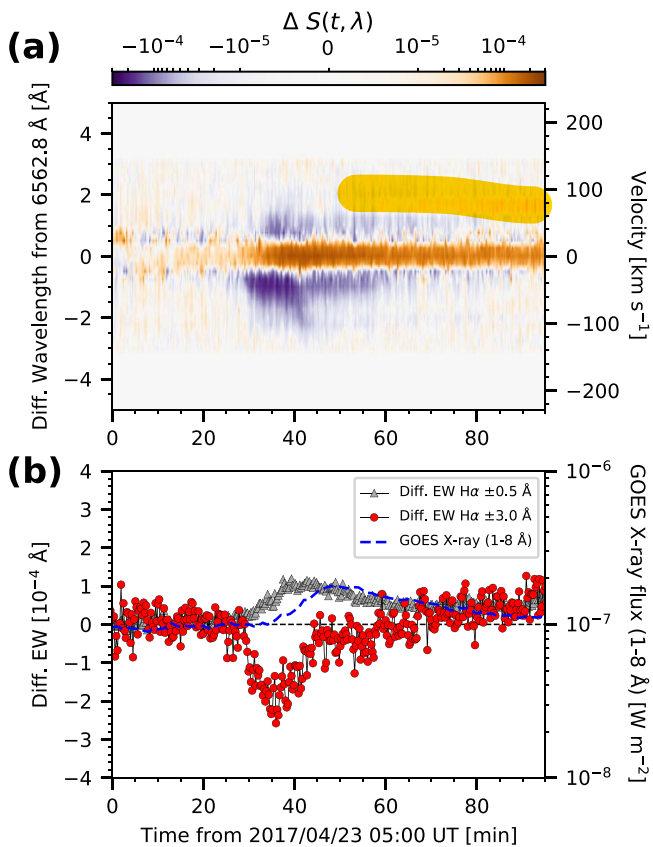
Figure 18 shows an overview of event (9). In this event, a prominence eruption to the outside of the solar limb occurred on 2021 May 5 22:25 UT (the orange dashed–dotted region in Figure 18(a)). We integrated  $H\alpha$  spectra over the region outside of the solar disk (the red dashed region in Figure 18(b)). The  $H\alpha$  flare ribbon is not seen from Earth, so the footpoints of this event must be on the backside of the solar limb, as for event (8).

Figure 19 shows the result of the Sun-as-a-star analysis of the  $H\alpha$  spectra of this prominence eruption. In the dynamic spectrum (Figure 19(a)), a blueshifted emission first appears. When this emission approaches the  $H\alpha$  line center, a second emission component appears, drifting from the blue wing to the red wing. In this event, two successive prominence eruptions occurred, and both erupted with their LOS velocities approaching Earth. After the second eruption, part of the prominence fell back into the solar surface, with the LOS velocity moving away from Earth. The successive emissions in the dynamic spectrum come from this series of plasma motions outside the solar limb. Corresponding to these successive emissions, the quantity  $\Delta EW_{H\alpha \pm 9.0 \text{ \AA}}$  for event (9) shows a two-step brightening (Figure 19(b)), with emission amplitudes  $\sim 1 \times 10^{-4} \text{ \AA}$  for the first one and  $\sim 2 \times 10^{-4} \text{ \AA}$  for the second one.

**Table 2**  
Summary of the Results of Sun-as-a-star Analysis

Event	Event Features	Features in Sun-as-a-star Spectra	$\pm\Delta\lambda$ (Å)	Em. (Å)	Abs. (Å)
(1)	Flare + surge	Em., shifted abs.	$\pm 3.0$	$3 \times 10^{-4}$	$2 \times 10^{-4}$
(2)	Flare + eruption	Em., blueshifted abs. (weak)	$\pm 3.0$	$4 \times 10^{-4}$	None
(3)	Flare (two step) + eruption	Em. (two step)	$\pm 3.0$	$4 \times 10^{-4}, 2 \times 10^{-4}$	None
(4)	Flare + coronal rain ?	Em., redshifted abs.	$\pm 3.0$	$1.5 \times 10^{-4}$	$0.5 \times 10^{-4}$
(5)	Filament eruption	Em., shifted abs.	$\pm 3.0$	$1 \times 10^{-4}$	$1 \times 10^{-4}$
(6)	Two-ribbon flare + filament eruption	Em., shifted abs.	$\pm 4.0$	$1 \times 10^{-4}$	$3 \times 10^{-4}$
(7)	Two-ribbon flare + filament eruption	Em., shifted abs.	$\pm 3.0$	$1 \times 10^{-4}$	$3 \times 10^{-4}$
(8)	Prominence eruption	Shifted em.	$\pm 3.0$	$3 \times 10^{-4}$	None
(9)	Prominence eruption (two step)	Shifted em. (two step)	$\pm 9.0$	$2 \times 10^{-4}, 1 \times 10^{-4}$	None

**Note.** In this Table, “Em.” and “Abs.” represent emission and absorption, respectively. In the columns labeled Em. (Å) and Abs. (Å), the approximate amplitudes of emissions and absorptions in differenced equivalent widths are shown, respectively. In the column labeled  $\pm\Delta\lambda$  (Å), we summarized the integral ranges used for calculating the differenced equivalent widths in the columns of Em. (Å) and Abs. (Å).



**Figure 15.** The same as Figure 2, but for event (7), the filament eruption and the two-ribbon flare on 2017 April 23. In addition to the differenced equivalent widths of  $H\alpha \pm 3.0$  Å, the differenced equivalent widths of  $H\alpha \pm 0.5$  Å are also plotted as gray triangles in panel (b), as in Figure 10(b) and Figure 13(b). We note that only  $H\alpha \pm 3.0$  Å data were available for performing the Sun-as-a-star analysis in this event.

## 5. Summary and Implications for Stellar Observations

We have performed Sun-as-a-star analyses of the  $H\alpha$  spectra of the various active events on the Sun; specifically, flares ( $\geq C8.0$ ), filament eruptions with large spatial scales and eruptions of off-limb prominences. Our aim is to increase the number of samples beyond those provided by Namekata et al. (2022a, 2022c)—who reported Sun-as-a-star analyses of a solar flare, a filament eruption, and a surge—and to clarify the correspondence between various active events and features

seen in Sun-as-a-star  $H\alpha$  spectra for future applications to stellar observations. We have summarized our results in Table 2. All nine events analyzed in this study show emission relative to the pre-event level. The amplitudes of their differenced equivalent widths are all on the order of  $10^{-4}$  Å, regardless of the cause of the emission. On the other hand, the dynamic spectra show different features, depending on the cause of the emission: (i) flares show emission at the  $H\alpha$  line center with red asymmetry and line broadening as reported in a previous study, (ii) filament eruptions with and without flares show emission near the  $H\alpha$  line center, together with blueshifted/redshifted absorptions, and (iii) eruptions of off-limb prominences show blueshifted/redshifted emissions. If spectral features similar to those of (i)–(iii) are obtained in stellar observations, we will thus be able to identify the phenomena occurring on those stars. We summarize below the details of the features in the Sun-as-a-star  $H\alpha$  spectra.

1. Flares ( $\geq C8.0$ ) show emission near the  $H\alpha$  line center, with red asymmetry and/or line broadening in their Sun-as-a-star  $H\alpha$  spectra. Namekata et al. (2022c) also reported that the Sun-as-a-star  $H\alpha$  spectrum of an M4.2 solar flare near the disk center showed red asymmetry and line broadening, and they thus suggested that the nature of the chromospheric condensation can be seen even in the Sun-as-a-star spectra. We note that, although event (2) and event (3) are especially energetic events in our study, red asymmetry is not very clear in them. These two events occurred near the solar limbs, and the lack of red asymmetry can be explained as a projection effect, as reported in previous studies (e.g., Švestka et al. 1962). The red asymmetry associated with flares can be interpreted as chromospheric condensation moving downward (e.g., Ichimoto & Kurokawa 1984; Asai et al. 2012). Therefore, assuming that material moves along a direction radial from the Sun, flares occurring near the solar limb should show a weak red asymmetry. In event (4), a redshifted absorption appears in the Sun-as-a-star  $H\alpha$  spectra when the emission due to the M1.1 flare almost decayed. This redshifted absorption during the flare-decay phase is the candidate for coronal rains from post-flare loops.
2. Filament eruptions with sufficient LOS velocity result in both emission at the  $H\alpha$  line center and shifted absorptions in the Sun-as-a-star  $H\alpha$  spectra. Emissions from flares in Sun-as-a-star  $H\alpha$  spectra have been

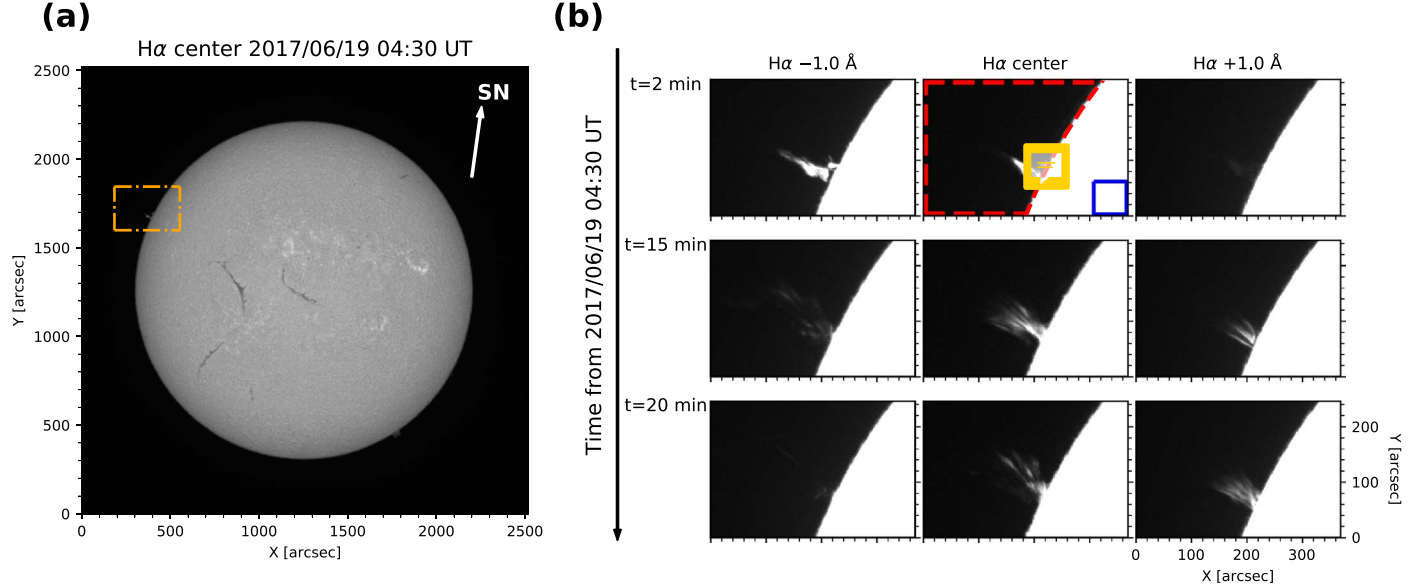


**Figure 16.** Overview of event (8), which occurred on 2017 June 19. (a) A full-disk solar image at the H $\alpha$ -center wavelength observed by SMART/SDDI. Celestial north is up, and west is to the right. The orange dashed–dotted region corresponds to the images in Figure 16(b). The direction of the solar north is shown by the white arrow labeled SN. (b) The time evolution of the filament eruption on 2017 June 19. The field of view in each panel corresponds to the orange dashed–dotted region in Figure 16(a). In each row, images at the times  $t = 2, 15$ , and  $20$  minutes measured from 04:30 UT 2017 June 19 are shown from top to bottom. In each column, the images H $\alpha$  -1.0 Å, H $\alpha$  center, and H $\alpha$  +1.0 Å are shown from left to right. The red dashed region in the H $\alpha$  center image at  $t = 2$  minutes is a TR, and the blue region is a QR.

reported previously by Namekata et al. (2022a, 2022c), but we found that additional apparent emission at the H $\alpha$  line center due to the disappearance of a dark filament. As shown in Figure 11, such apparent emission can be comparable to emission due to a two-ribbon flare and it can contribute to the H $\alpha$  spectral-line formation. Before fast eruptions, slow blueshifted absorptions appear in the Sun-as-a-star H $\alpha$  spectra (clearly seen in event (6), Figure 13(a)). These absorptions probably come from slow motions of the filaments before the eruptions, as reported in many previous studies with spatially resolved images (Sterling & Moore 2004; Isobe & Tripathi 2006; Seki et al. 2017, 2019a). In addition to the blueshifted absorption due to upward motions of the filaments, redshifted absorptions appear together with the emissions in the dynamic spectra. These redshifted absorptions come from partial drainage of the erupting filaments.

- Prominence eruptions that erupted outside the solar limb result in shifted emission in the Sun-as-a-star H $\alpha$  spectra. It is well known from spatially resolved viewpoints, that when a prominence erupts beyond the solar limb, emission occurs in the H $\alpha$  spectra because of the absence of background light (Parenti 2014). The prominences of event (8) and event (9) have velocities along the LOS direction, and the shifted emissions therefore appear in the Sun-as-a-star H $\alpha$  spectra. We demonstrate for the first time how the H $\alpha$  spectra of prominence eruption can be seen in the Sun-as-a-star view.

We also compared the time evolution of H $\alpha$  differedenced equivalent widths and GOES soft X-ray data. In events (1)–(4) (flares), the light curves of H $\alpha$  and GOES soft X-ray are similar in the timescales of the impulsive phases and the peak times. This similarity is consistent with the standard flare model in which both H $\alpha$  and soft X-ray emissions are related to chromospheric bombardment. On the other hand, in decay phases H $\alpha$  light

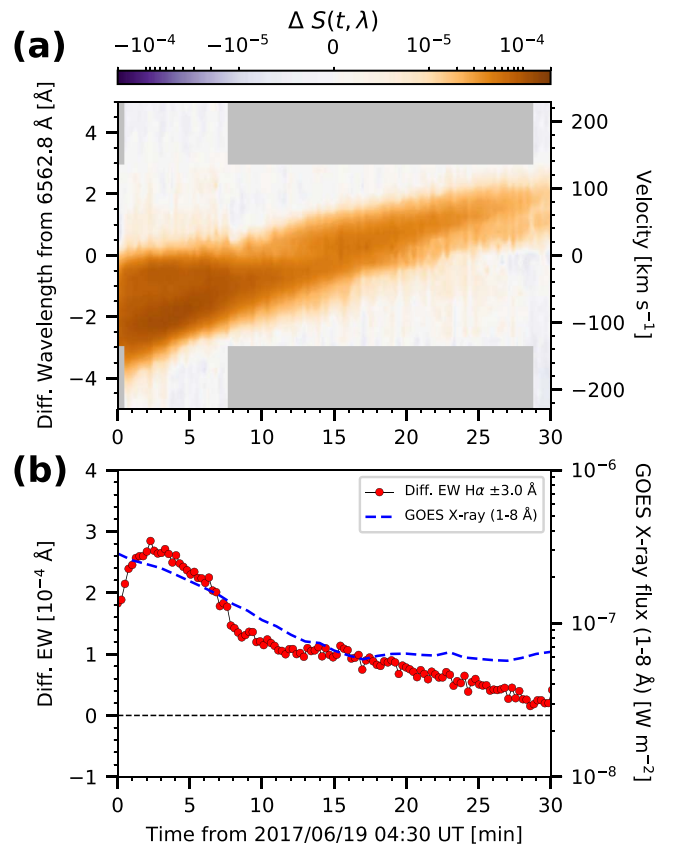


**Figure 17.** The same as Figure 2, but for event (8), the prominence eruption on 2017 June 19. We note that the peak time of GOES soft X-ray (1–8 Å) is before 2017 June 19 04:30 UT.

curves sometimes show absorption due to LOS motions of plasmas as previously reported by Namekata et al. (2022a) and differ from soft X-ray light curves (especially in Figures 2(b) and

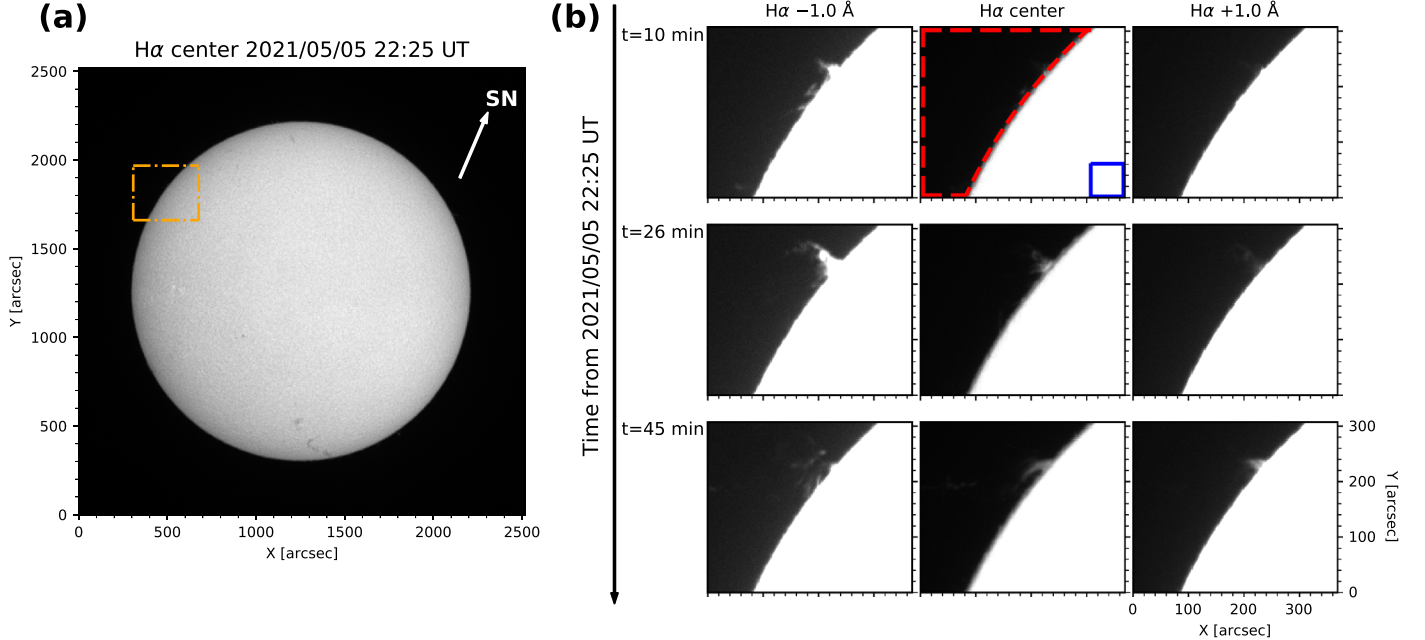


**Figure 18.** Overview of event (9), which occurred on 2021 May 5. (a) A-full-disk solar image at the H $\alpha$ -center wavelength observed by SMART/SDDI. Celestial north is up, and west is to the right. The orange dashed–dotted region corresponds to the images in Figure 18(b). The direction of the solar north is shown by the white arrow labeled SN. (b) The time evolution of the filament eruption on 2021 May 5. The field of view in each panel corresponds to the orange dashed–dotted region in Figure 18(a). In each row, images at the times  $t = 10, 26$ , and  $45$  minutes measured from 22:25 UT on 2021 May 5 are shown from top to bottom. In each column, the images of H $\alpha$   $-1.0 \text{ \AA}$ , H $\alpha$  center, and H $\alpha$   $+1.0 \text{ \AA}$  are shown from left to right. The red dashed region in the H $\alpha$  center image at  $t = 10$  minutes is a TR, and the blue solid region is a QR.

8(b)). For the same reason, in events (5)–(7) (filament eruptions), H $\alpha$  light curves including both emission and absorption differ from soft X-ray light curves (red circles in Figures 10(b), 13(b), and 15(b)). In events (8) and (9) (prominence eruption), the peak time of H $\alpha$  delayed that of soft X-ray (Figures 17(b) and 19(b)). The flare footpoints were occulted in these two events and H $\alpha$  emissions are purely caused by eruptions of off-limb prominences. It takes much time for the prominence to expand to occupy a large area so the H $\alpha$  peak lagged behind the soft X-ray peak. This time lag may be the key to identifying whether H $\alpha$  emission comes from a flare or a prominence eruption but more statistics are needed to confirm its universality.

We highlight another important result: the cancellation between the emission due to an M5.3-class flare that occurred on the solar limb and the absorption due to the filament eruption. Out of the four flare events ( $\geq C8.0$ ), events (1)–(3) were associated with H $\alpha$  filament eruptions. In the dynamic spectrum of event (1), which occurred near the disk center, clear absorption signals appear that correspond to a surge. In contrast, the dynamic spectra of event (2) and event (3), which occurred around the limb, do not show clear absorptions. For event (2), the absorption caused by the eruption on the solar disk was canceled or decreased by the flare emission near the H $\alpha$  line center because of the small LOS velocity of the filament. On the other hand, some stellar flares show drastically broad emissions in their H $\alpha$  spectra (e.g., Namekata et al. 2020 reported that a superflare on the M dwarf AD Leonis exhibited an H $\alpha$  line width up to  $14 \text{ \AA}$ ). Such broad emissions can cancel or decrease absorptions from filament eruptions with high LOS velocities. Thus, we deduce that for some stellar (super-) flares with broad H $\alpha$  emissions, filament eruptions on the stellar disks may not be detected in the H $\alpha$  spectra, even if filaments have high LOS velocities.

As mentioned in summary (i), relatively prominent flares ( $\geq C8.0$ ) showed red asymmetry as signatures of chromospheric condensation in their impulsive phases. Such red asymmetry has been observed in other chromospheric lines. For example, Graham et al. (2020) analyzed the impulsive phase of an X-class solar flare and they reported that multiple chromospheric lines of Fe I, Fe II, Mg II, C I, and Si II all showed red asymmetry. They also performed a radiative hydrodynamic simulation and showed that the red asymmetry can be explained by the collision of the electron beam with the solar chromosphere. In addition, Tian & Chen (2018) reported that the transition-region line of Si IV showed red asymmetry persisting in both impulsive and decay phases of an M-class solar flare. As for the stellar case, Woodgate et al. (1992) reported that a stellar flare on the red dwarf star AU Mic showed red asymmetry in Ly $\alpha$  during the impulsive phase. This stellar observation suggests that chromospheric condensation also occurs during the impulsive phases of stellar flares.

Seki et al. (2019b) provided the catalog of filament disappearance observed by SMART/SDDI, and they reported that the three filament eruptions in event (4), event (5), and event (6) evolved to become CMEs. On the other hand, the present study showed that redshifted absorptions, which come from falling plasmas, appear in the Sun-as-a-star H $\alpha$  spectra of these three events. This suggests that even if falling plasmas are detected as redshifted absorptions in the observations of stellar filament eruptions, such filament eruptions may also develop into CMEs. We need further investigation to clarify whether we can deduce the occurrence of CMEs from spatially integrated H $\alpha$  spectra.

In recent stellar observations, some H $\alpha$  spectra of stellar flares on M/K dwarfs exhibited emission with blue asymmetry (e.g., Vida et al. 2016, 2019; Muheki et al. 2020; Maehara et al. 2021). They proposed that a prominence eruption caused the

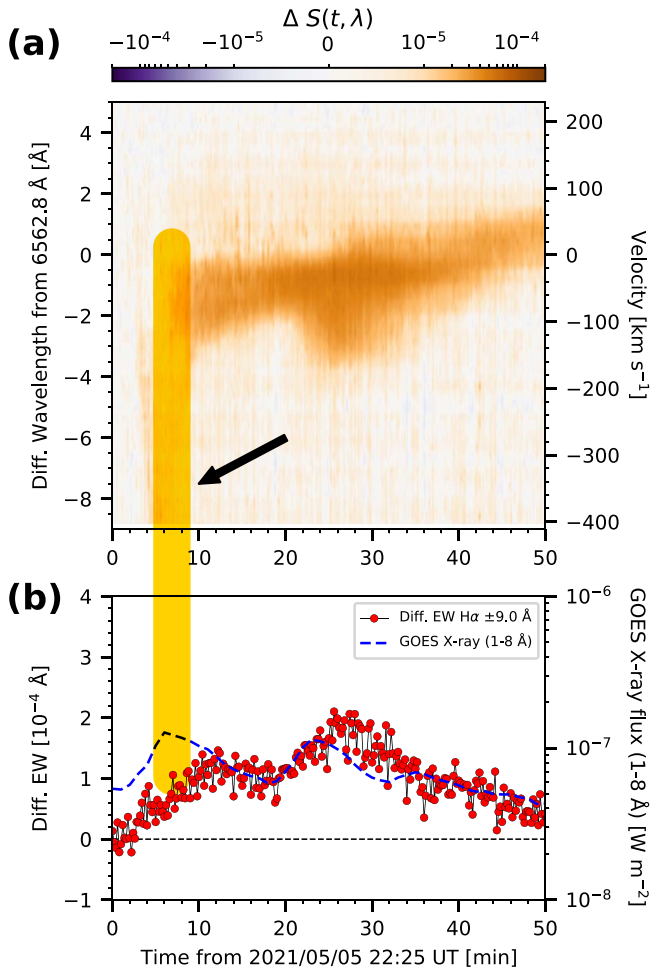


**Figure 19.** The same as Figure 2, but for event (9), the prominence eruption on 2021 May 5. In order to cover the fast component of the first eruption, we extended the range of the blue wing to  $-9.0 \text{ \AA}$  in panel (a). The black arrow in panel (a) indicates a fast component of this eruption.

blue asymmetry in their study. They considered that emission along the H $\alpha$  line center due to the superflare and blueshifted emission due to the prominence eruption moving toward Earth may overlap to produce such emissions with the blue asymmetry. In the present study, we found that solar prominences erupting toward Earth also resulted in blueshifted emissions in the Sun-as-a-star H $\alpha$  spectra. Moreover, the amplitudes of these blueshifted emissions were comparable to those of solar flares ( $C8.0 \leq \text{flare class} \leq M8.1$ ). This suggests that if we observe flares with prominence eruptions, such prominence eruptions can make non-negligible contributions to the formation of the H $\alpha$  spectra. Thus, our results for solar-prominence eruptions support the suggestion that the blue asymmetry may come from prominence eruptions. In the future, Sun-as-a-star analyses are needed for a solar-prominence eruption with a footpoint flare in order to investigate whether prominence eruptions really can cause the blue asymmetry observed in the stellar cases.

In event (9), the emission with high velocity up to  $-9.0 \text{ \AA}$  for the first eruption is fainter than the emission with small velocity, in the Sun-as-a-star H $\alpha$  dynamic spectrum (Figure 19(a)). We have considered that since the fast plasmas in this event occupied only a small spatial scale, their contributions to the emission in the spatially integrated spectra

became much smaller than the contributions from the slow plasmas, which had large spatial scales. For stellar observations, in which the number of photons is much smaller than that for the Sun, emission from faster but smaller blobs of plasma may become invisible in the spatially integrated observational data. This suggests that even if high-velocity emission is not recognized in stellar H $\alpha$  spectra, faster plasma may still exist in stellar active phenomena.

The relationship between flare energy (e.g., X-ray fluence) and CME kinetic energy has been previously investigated (e.g., Yashiro & Gopalswamy 2009). On the other hand, the relationship between flare energy and kinetic energy of filament eruption is not clear. In the present paper, there is not enough data to discuss it, but their relation should be investigated by increasing the number of samples.

As shown in this study, the signals of active events generally survive in spatially integrated H $\alpha$  spectra. This means that time-resolved H $\alpha$  spectroscopic observations are strong tools for distinguishing what the stellar active events look like. However, the signals of some active events in H $\alpha$  spectra may be suppressed by cancellation between emissions and absorptions, as occurred in event (2). This suggests that in addition to H $\alpha$  observations, the observations of other wavelengths are necessary to deduce the stellar activities more accurately. Also, the comparison of the H $\alpha$  line and another wavelength such as EUV is useful to investigate signals of CMEs in spatially integrated H $\alpha$  spectrum (Harra et al. 2016; Xu et al. 2022). Multiwavelength spectroscopy from the Sun-as-a-star viewpoint will be necessary to achieve a deeper understanding of various active events on stars.

The authors thank the anonymous referee for constructive comments that significantly improved the quality of this paper. We wish to thank Drs. K. Shibata and Y. Notsu for fruitful discussions. We express our sincere gratitude to the staff of the Hida Observatory for the development and maintenance of the instrument and daily observation. We would like to acknowledge the data used from GOES, SDO, and SOHO. SDO is a mission for NASA's Living With a Star program. This research was carried out by the joint research program of the Institute for Space-Earth Environmental Research, Nagoya University. This research is supported by JSPS KAKENHI grant No. 21H01131 (K.I. and A.A.) and 18J20048, 21J00316 (K.N.). The authors would like to thank Enago for the English language review.

*Software:* astropy (Astropy Collaboration et al. 2018), sunpy (The SunPy Community et al. 2020).

## ORCID iDs

Kiyoshi Ichimoto <https://orcid.org/0000-0001-8689-3564>  
Kosuke Namekata <https://orcid.org/0000-0002-1297-9485>

## References

- Airapetian, V. S., Barnes, R., Cohen, O., et al. 2020, *IJAsB*, **19**, 136
- Asai, A., Ichimoto, K., Kita, R., Kurokawa, H., & Shibata, K. 2012, *PASJ*, **64**, 20
- Astropy Collaboration, Price-Whelan, A. M., Sipőcz, B. M., et al. 2018, *AJ*, **156**, 123
- Brueckner, G. E., Howard, R. A., Koomen, M. J., et al. 1995, *SoPh*, **162**, 357
- Cliver, E. W., Schrijver, C. J., Shibata, K., & Usoskin, I. G. 2022, *LRSP*, **19**, 2
- Graham, D. R., Cauzzi, G., Zangrilli, L., et al. 2020, *ApJ*, **895**, 6
- Harra, L. K., Schrijver, C. J., Janvier, M., et al. 2016, *SoPh*, **291**, 1761
- Honda, S., Notsu, Y., Namekata, K., et al. 2018, *PASJ*, **70**, 62
- Ichimoto, K., Ishii, T. T., Otsuji, K., et al. 2017, *SoPh*, **292**, 63

- Ichimoto, K., & Kurokawa, H. 1984, *SoPh*, **93**, 105  
 Isobe, H., & Tripathi, D. 2006, *A&A*, **449**, L17  
 Jing, J., Xu, Y., Cao, W., et al. 2016, *NatSR*, **6**, 24319  
 Kowalski, A. F., Hawley, S. L., Wisniewski, J. P., et al. 2013, *ApJS*, **207**, 15  
 Lemen, J. R., Title, A. M., Akin, D. J., et al. 2012, *SoPh*, **275**, 17  
 Maehara, H., Notsu, Y., Namekata, K., et al. 2021, *PASJ*, **73**, 44  
 Maehara, H., Shibayama, T., Notsu, S., et al. 2012, *Natur*, **485**, 478  
 Muheki, P., Guenther, E. W., Mutabazi, T., et al. 2020, *A&A*, **637**, A13  
 Namekata, K., Ichimoto, K., Ishii, T. T., & Shibata, K. 2022c, *ApJ*, **933**, 209  
 Namekata, K., Maehara, H., Honda, S., et al. 2022a, *NatAs*, **6**, 241  
 Namekata, K., Maehara, H., Honda, S., et al. 2022b, *ApJL*, **926**, L5  
 Namekata, K., Maehara, H., Sasaki, R., et al. 2020, *PASJ*, **72**, 68  
 Notsu, Y., Maehara, H., Honda, S., et al. 2019, *ApJ*, **876**, 58  
 Okamoto, S., Notsu, Y., Maehara, H., et al. 2021, *ApJ*, **906**, 72  
 Parenti, S. 2014, *LRSP*, **11**, 1  
 Pesnell, W. D., Thompson, B. J., & Chamberlin, P. C. 2012, *SoPh*, **275**, 3  
 Rumph, T., Bowyer, S., & Vennes, S. 1994, *AJ*, **107**, 2108  
 Seki, D., Otsuji, K., Ishii, T., et al. 2019b, *SunGe*, **14**, 95  
 Seki, D., Otsuji, K., Isobe, H., et al. 2017, *ApJL*, **843**, L24  
 Seki, D., Otsuji, K., Isobe, H., et al. 2019a, *PASJ*, **71**, 56  
 Shibata, K., & Magara, T. 2011, *LRSP*, **8**, 6  
 Shibayama, T., Maebara, H., Notsu, S., et al. 2013, *ApJS*, **209**, 5  
 Sterling, A. C., & Moore, R. L. 2004, *ApJ*, **602**, 1024  
 Švestka, Z., Kopecký, M., & Blaha, M. 1962, BAICz, **13**, 37  
 The SunPy Community, Barnes, W. T., Bobra, M. G., et al. 2020, *ApJ*, **890**, 68  
 Tian, H., & Chen, N.-H. 2018, *ApJ*, **856**, 34  
 Toriumi, S., & Airapetian, V. S. 2022, *ApJ*, **927**, 179  
 Toriumi, S., Airapetian, V. S., Hudson, H. S., et al. 2020, *ApJ*, **902**, 36  
 Tsuboi, Y., Yamazaki, K., Sugawara, Y., et al. 2016, *PASJ*, **68**, 90  
 Tu, Z.-L., Yang, M., Zhang, Z. J., et al. 2020, *ApJ*, **890**, 46  
 Ueno, S., Nagata, S., Kitai, R., et al. 2004, in ASP Conf. Ser. 325, The Solar-B Mission and the Forefront of Solar Physics (San Francisco, CA: ASP), **319**  
 Veronig, A. M., Odert, P., Leitzinger, M., et al. 2021, *NatAs*, **5**, 697  
 Vida, K., Kriskovics, L., Oláh, K., et al. 2016, *A&A*, **590**, A11  
 Vida, K., Oláh, K., Kovári, Z., et al. 2019, *ApJ*, **884**, 160  
 Woodgate, B. E., Robinson, R. D., Carpenter, K. G., et al. 1992, *ApJL*, **397**, L95  
 Xu, Y., Tian, H., Hou, Z., et al. 2022, *ApJ*, **931**, 76  
 Yashiro, S., & Gopalswamy, N. 2009, in IAU Symp. 257, Universal Heliospheric Processes (Cambridge: Cambridge Univ. Press), **233**